A&A 649, A164 (2021)
https://doi.org/10.1051/0004-6361/202039592
© ESO 2021

Astronomy & Astrophysics

Fast outflows in protoplanetary nebulae and young planetary nebulae observed by *Herschel*/HIFI⋆

M. Lorenzo[1,⋆⋆], D. Teyssier[2], V. Bujarrabal[3], P. García-Lario[1], J. Alcolea[4], E. Verdugo[1], and A. Marston[1]

[1] European Space Astronomy Centre, ESA, PO Box 78, 28691 Villanueva de la Cañada, Madrid, Spain
e-mail: malore06@ucm.es
[2] Telespazio Vega UK Ltd. for ESA/ESAC, Madrid, Spain
[3] Observatorio Astronómico Nacional (IGN), Ap 112, 28803 Alcalá de Henares, Spain
[4] Observatorio Astronómico Nacional (OAN-IGN), Calle Alfonso XII 3, 28014 Madrid, Spain

Received 5 October 2020 / Accepted 2 April 2021

ABSTRACT

Context. Fast outflows and their interaction with slow shells (generally known as the fossil circumstellar envelope of asymptotic giant branch stars) play an important role in the structure and kinematics of protoplanetary and planetary nebulae (pPNe, PNe). To properly study their effects within these objects, we also need to observe the intermediate-temperature gas, which is only detectable in the far-infrared and submillimetre (submm) transitions.
Aims. We study the physical conditions of the outflows presented in a number of pPNe and PNe, with a focus on their temperature and excitation states.
Methods. We carried out *Herschel*/HIFI observations in the submm lines of ^{12}CO in nine pPNe and nine PNe and complemented them with low-J CO spectra obtained with the IRAM 30m telescope and taken from the literature. The spectral resolution of HIFI allows us to identify and measure the different nebular components in the line profiles. The comparison with large velocity gradient model predictions was used to estimate the physical conditions of the warm gas in the nebulae, such as excitation conditions, temperature, and density.
Results. We found high kinetic temperatures for the fast winds of pPNe, typically reaching between 75 K and 200 K. In contrast, the high-velocity gas in the sampled PNe is colder, with characteristic temperatures between 25 K and 75 K, and it is found in a lower excitation state. We interpret this correlation of the kinetic temperature and excitation state of fast outflows with the amount of time elapsed since their acceleration (probably driven by shocks) as a consequence of the cooling that occurred during the pPN phase.

Key words. stars: AGB and post-AGB – circumstellar matter – stars: mass-loss – planetary nebulae: general

1. Introduction

Throughout the very short post-AGB phase, lasting less than a few thousand years, a dramatic change occurs in the morphology and dynamics of the circumstellar envelopes (CSEs) of evolved stars of intermediate mass. Starting from an intense mass-loss period that results in the formation of a dense, spherical, and slowly expanding CSE, asymptotic giant branch (AGB) stars then turn into the central stars of planetary nebulae (PNe). These PNe present complex morphological structures, often with strong axial-symmetry. These extreme kinetic and morphological changes are thought to arise from the interaction between fast, collimated (jet-like) winds and the slow, dense layers of the CSE. The transformation takes place in the intermediate stage known as the protoplanetary nebula (pPN) phase.

Collimated winds, commonly known as fast outflows, are ejected close to the central core and carry a significant fraction of nebular mass, that is, ∼0.1–0.3 $M_\odot$ (Bujarrabal et al. 2001), with velocities around 100 km s^{-1}. The interaction between these fast outflows and the remnant of the slowly expanding circumstellar envelope (AGB-CSE) is believed to be the main agent responsible for the change of kinematics and structure observed in pPNe, sculpting the final shape of PNe (Balick & Frank 2002). Several observations of molecular lines have identified fast outflows in many pPNe and PNe; see examples in Bujarrabal et al. (1998, 2001), Alcolea et al. (2001), Castro-Carrizo et al. (2002), Sánchez Contreras et al. (2004), Fong et al. (2006), and references therein. In most cases, they exhibit strong emission of molecular lines with composite profiles. Typically, these profiles consist of a central core that comes from the earlier slow AGB wind and broad line wings arising from fast post-AGB outflows. In molecular line emission, these outflows show bipolar or hourglass-like geometries and dynamics in almost all well-studied cases, although the optical images of many PNe and pPNe tend to be more complex, with multipolar or point-like symmetries.

Until now, most of what we know about the structure, dynamics, and physical conditions of molecular material in nebulae has been derived mainly from observations of low-J transitions of molecular lines, especially the $J = 2$–1 and $J = 1$–0 transitions of CO. These lines primarily trace molecular gas in the cold, (typically) outer layers of the circumstellar envelope, where the expansion velocity is already constant and the temperature, as it is decreasing with the radius as ∼1/r, typically reaches between 10–20 K. There are also many studies

⋆ A copy of the reduced spectra is only available at the CDS via anonymous ftp to cdsarc.u-strasbg.fr (130.79.128.5) or via http://cdsarc.u-strasbg.fr/viz-bin/cat/J/A+A/649/A164
⋆⋆ Currently at Centro de Astrobiología (CSIC-INTA), Torrejón de Ardoz, Madrid, Spain.

analysing molecules with higher dipole moments, such as HCN, HCO+, and HNC, which trace denser gas than CO (e.g., Bachiller et al. 1997; Zhang & Kwok 2008; Milam et al. 2009; Edwards & Ziurys 2013; Edwards et al. 2014; Schmidt & Ziurys 2016; Bublitz et al. 2019, and references therein). However, to completely understand the shaping mechanism of the highly collimated jets in pPNe and PNe, and, consequently, their evolution, we also need to observe warmer regions ($100\,\mathrm{K} \lesssim T_K \lesssim 1000\,\mathrm{K}$), which is where acceleration takes place. A proper study of intermediate-temperature gas requires observations of higher J transitions of CO that are found in the far-infrared (FIR) and submillimetre (submm) ranges.

Unfortunately, there are very few studies based on the observation of the molecular gas of pPNe and PNe in the FIR and submm lines. Justtanont et al. (2000) were the first to analyse the intermediate-temperature gas around evolved stars in the FIR. They presented ISO-LWS observations of high-J transitions of CO (from $J = 14$–13 up to $J = 37$–36) in CRL 618, CRL 2688 and NGC 7027, but the low spectral resolution of their data prevented them from identifying the nebular components responsible for the line emission. Higher spectral resolution was achieved with *Herschel* in the FIR/submm observations presented in Bujarrabal et al. (2012). By comparing their results with theoretical predictions, they found warm fast winds in CRL 618 and CRL 2688 ($T_k \geq 100\,\mathrm{K}$) and colder outflows in OH 231+4.2 and NGC 6302 ($T_k \sim 30\,\mathrm{K}$).

Herschel, and in particular its HIFI heterodyne spectrometer, provides the necessarily high spectral resolution ($\frac{\Delta v}{v} < 10^{-6}$) in the FIR and submm to determine the dynamics and physical conditions of the shocked layers of this type of nebulae and to resolve the different features of their profiles. In this paper, we present observations of intermediate-excitation CO lines in a sample of eighteen nebulae carried out with HIFI. These observations have been obtained as part of the guaranteed-time project SUbmilimetre Catalogue of Circumstellar Envelopes of StarS (SUCCESS), a submm/FIR CO survey of a large sample of AGB and post-AGB stars. In particular, this programme obtained observations of the ^{12}CO $J = 5$–4 and $J = 9$–8 lines in 18 post-AGB stars. Of this sample of nebulae, three were also observed in the ^{12}CO $J = 14$–13 line and five were followed up in ^{12}CO $J = 2$–1 and $J = 1$–0 lines using the IRAM 30m telescope.

2. Observations

2.1. Herschel/HIFI observations

Observations in the submm lines of CO were obtained in the context of the *Herschel* SUCCESS Guaranteed Time project (Teyssier et al. 2011) executed with the HIFI high-resolution spectrometer (de Graauw et al. 2010). The post-AGB stars considered in this paper represent about a quarter of the whole sample observed by this programme. Details on how the data were acquired and processed can be found in Danilovich et al. (2015). No particular spectral smoothing was applied to the data for their analysis, however, rebinning was applied in some of the spectra given in the paper.

2.2. Supplementary data

Our HIFI data were complemented with low-J CO spectra obtained during an observing campaign at the IRAM 30m telescope, aimed at getting better calibrated data for some of the sources where the only available spectra had been taken several decades ago. These observations were conducted in December 2012 and comprised five sources from our sample of post-AGB stars. For the rest of the sources, we relied on data digitised from the literature or unpublished data available to members of our team. Table 1 summarises the origin of the spectra used in this paper for the low-excitation CO lines. The corresponding spectra are shown in Appendix A. In the analysis described in Sect. 4, we distinguish among the compact and extended sources and we provide examples of the information shown together with the spectra of these sources in Figs. 1 and 2, respectively. For some sources, spectra are also given for additional CO transitions (e.g., Fig. A.9). These were used in support to the selection of the velocity ranges applied in our analysis (Sect. 4.1).

Table 1. Details on the origin of the low-J CO spectra used in this study.

Source	CO $J = 1$–0	CO $J = 2$–1
IRAS 07134+1005	Bujarrabal et al. (1992) [a]	
IRAS 19500–1709	Bujarrabal (priv. comm.) [a]	
IRAS 21282+5050	Castro-Carrizo et al. (2010) [a,b]	
IRAS 22272+5435	Bujarrabal (priv. comm.) [a]	
M 1–92	New 30m data	
M 2–56	Bujarrabal (priv. comm.) [a]	
OH 17.7–2.0	Sánchez Contreras et al. (2007) [c]	Heske et al. (1990) [a]
R Sct	Bujarrabal (priv. comm.) [a]	
89 Her	Bujarrabal (priv. comm.) [a]	
NGC 6537	New 30m data	
M 1–16	New 30m data	
M 1–17	New 30m data	
M 3–28	New 30m data	
NGC 2346	Bachiller et al. (1989) [a]	
NGC 6072	Cox et al. (1992) [d]	
NGC 6720	Bachiller et al. (1989) [a]	
NGC 6781	Bachiller et al. (1993) [a]	
NGC 7293	Zack & Ziurys (2013) [e]	Young et al. (1999) [f]

Notes. [a]IRAM 30 m telescope, [b]IRAM Plateau de Bure interferometer, [c]OVRO interferometer, [d]SEST telescope, [e]ARO 12 m telescope, [f]CSO 10.4 m telescope.

In two cases (IRAS 21282+5050 and OH17.7–2.0), the CO data stem from interferometric observations as no single-dish counterpart could be found in the literature. The two sources concerned by these observations are either compact (OH 17.7–2.0), or their interferometric data were combined with short spacings obtained at the 30m (IRAS 21282+5050). We have therefore assumed that there is no significant flux loss in the corresponding data. The conversion from surface brightness to temperature units we used were: $45\,\mathrm{mK\,Jy^{-1}\,beam^{-1}}$ (CO $J = 1$–0) and $29\,\mathrm{mK\,Jy^{-1}\,beam^{-1}}$ (CO $J = 2$–1) for the IRAM Plateau de Bure observations of Castro-Carrizo et al. (2010), and $1.19\,\mathrm{K\,Jy^{-1}\,beam^{-1}}$ (CO $J = 1$–0) for the OVRO observations of Sánchez Contreras et al. (2007).

3. Description of the sample

Our sample is presented in Table 3, alongside with their observed coordinates and other parameters. It consists of 18 post-AGBs: nine protoplanetary nebulae and nine planetary nebulae. Five of the PNe are considered extended sources with respect to the size of the HIFI beams (see their values in Table 2). In this section, we present a brief description of each source and a qualitative analysis of their observed CO profiles.

3.1. IRAS 07134+1005

IRAS 07134+1005 (HD 56126) is a pPN with a double-peaked SED (Kwok et al. 1989), presenting a high abundance

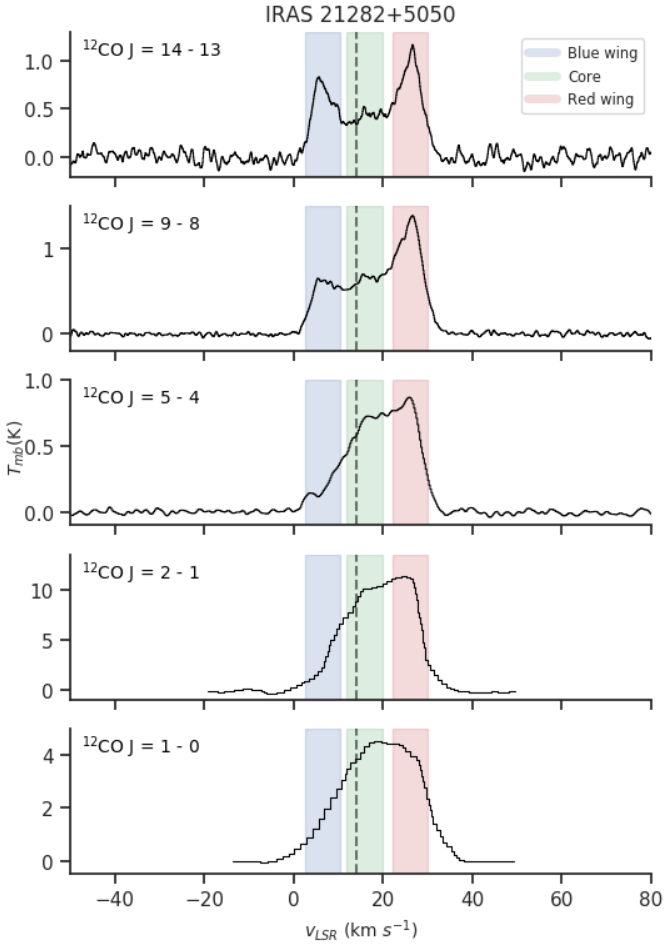


Fig. 1. Observations of IRAS 21282+5050. Shadowed regions mark the LSR velocity ranges adopted to determine the characteristic intensity of each feature. The dashed vertical lines indicates the systemic velocity as tabulated in Table 3.

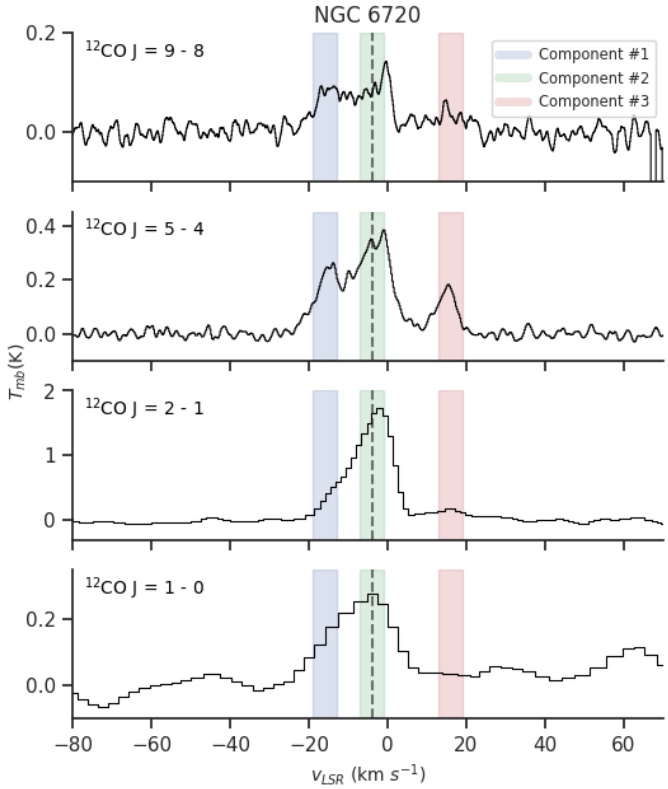


Fig. 2. Observations of NGC 6720. The shadowed regions indicate the velocity ranges adopted to determine the characteristic intensity of the detected velocity components; see Sect. 4.1 for further details.

of s-process elements, a typical characteristic of post-AGBs that have experienced the third dredge-up. Mid-IR images of IRAS 07134+1005 (Meixner et al. 1997) show an elliptical detached shell surrounding two aligned peaks, which these authors interpreted as limb-brightened peaks of a shell with an equatorial density enhancement. The profile of the CO $J = 9$–8 line obtained in our observations shows a double peak around the line core, indicative of high-velocity shocks (Fig. A.1).

3.2. IRAS 19500–1709

IRAS 19500–1709 (HD 187885) is a carbon-rich pPN. The high abundance of s-process elements in its shell and a feature at 21 μm in its spectra (Van Winckel & Reyniers 2000) suggests that the third dredge-up has already occurred in this object. IRAS 19500–1709 has a bi-modal spectral energy distribution (SED) characteristic of pPN with detached circumstellar dust envelope (Hrivnak et al. 1989). Our observed lines reflect this composite structure. They show, in most of them, a central line core (with an expansion velocity of 11 km s^{-1}) and wide line wings whose expansion velocity goes up to ∼30 km s^{-1}. Figure A.2 shows that the contribution from the remnant of the slow AGB wind is dominating the profile at low J, but then decreases significantly in the $J = 5$–4 line and above. This suggests that the temperature of the fast outflows is high in contrast with the slow expanding AGB-CSE. In addition, we can see a clear absorption in the blue wing of $J = 2$–1 line, supporting the idea that the fast component presents higher temperatures than the slow gas and that it is found closer to the central star.

3.3. IRAS 21282+5050

IRAS 21282+5050 is a young, C-rich protoplanetary nebula. The CO $J = 1$–0 maps by Shibata et al. (1989) show a clumpy expanding shell whose nature was interpreted as an expanding toroidal structure with an axis along the east-west direction, perpendicular to the line of sight. The spectra of the lower-energy transitions displayed in Fig. 1 exhibit profiles dominated by a roughly symmetric component around the systemic velocity. However, as the energy of the transition increases, the profile seems more of a composite as well as steep-sided, revealing the three typical features: two line wings growing in intensity with increasing J and a line-core decreasing with the excitation, indicative of a high temperature in the object's outflows.

3.4. IRAS 22272+5435

IRAS 22272+5435 (HD 235858) is a C-rich pPN (Kwok et al. 1989; Omont et al. 1995). Studies at optical (Ueta et al. 2000) and near-infrared (Gledhill et al. 2001) wavelengths have identified an axisymmetric nature (PA ∼ −35°) for the nebula and a toroidal dust shell normal to the axis. Maps of CO $J = 1$–0 (Fong et al. 2006) have shown that its molecular gas expands following a spherical structure with multiple protrusions in a quadrupolar geometry. As can be seen in Fig. A.3, its profile

Table 2. Frequencies and telescope parameters for the CO transitions used in this work.

Transition	Frequency (GHz)	Telescope	θ ($''$)
^{12}CO $J = 1$–0	115.271	IRAM	21.4
		PdBI	4.9×3.9
		OVRO	10.9×7.1
		SEST	45
		ARO	55
^{12}CO $J = 2$–1	230.538	IRAM	10.7
		PdBI	2.6×1.4
		SEST	23
		CSO	31
^{12}CO $J = 3$–2	345.796	APEX	17.3
		ARO SMT	22
^{12}CO $J = 4$–3	461.041	ARO SMT	16
^{12}CO $J = 5$–4	576.268	HIFI	36.1
^{12}CO $J = 6$–5	691.473	HIFI	30.4
		ARO SMT	11
^{12}CO $J = 9$–8	1036.912	HIFI	20.1
^{12}CO $J = 10$–9	1151.985	HIFI	18.2
^{12}CO $J = 14$–13	1611.794	HIFI	12.9
^{12}CO $J = 16$–15	11841.345	HIFI	11.5

Notes. IRAM is the 30 m telescope at the Institute de Radioastronomie Millimétrique; PdBI refers to the IRAM Plateau de Bure interferometer (now known as NOEMA); OVRO refers to the millimeter interferometer of the Owens Valley Radio Observatory; SEST is the 15 m Swedish-ESO Sub-millimeter Telescope; ARO refers to the 12 m telescope of the Arizona Radio Observatory; CSO is the 10.4 m Leighton telescope of the Caltech Submilimeter Observatory; ARO SMT is the 10 m Sub-millimeter Telescope of the Arizona Radio Observatory; APEX refers to the Atacama Pathfinder EXperiment; and HIFI is the Heterodyne Instrument for the Far-Infrared aboard *Herschel*.

displays a parabolic-like shape as commonly observed in AGB profiles.

3.5. M 1–92

M 1–92, also known as Minkowski's Footprint, is a very well studied O-rich pPN that presents OH masers. It shows a clear hourglass-like structure consisting of a thin flat disk expanding radially and two symmetrical lobes (Alcolea et al. 2007). The CO maps show that most of its molecular gas is located in the equatorial disk and in the walls of two empty lobules, where high velocities are observed (Bujarrabal et al. 1998). Figure A.4 shows intermediate velocity features that disappear as the energy levels increase.

3.6. M 2–56

M 2–56 is a pPN with a bipolar appearance in the optical and an hourglass-like shape in CO maps. These maps show a dense ring probably arising from the fossil AGB envelope and two high-velocity components at 11$''$–15$''$ from the centre along the symmetry axis. It also presents two empty attached shells close to the equatorial disk, expanding along the nebula axis at low velocities (Castro-Carrizo et al. 2002). As we can seen in Fig. A.5, the CO lines of M 2–56 are composite with a strong blue wing that remains as the dominant feature of the spectral profile at high values of J. This remarkable difference between the blue and the red wings is probably due to an intrinsic asymmetry.

3.7. OH 17.7–2.0

OH17.7–2.0 (IRAS 18276+143) is an OH/IR pPN that presents a double-peaked SED indicative of a detached dust shell (Le Bertre 1987). Polarised intensity images (Gledhill 2005) have found hourglass-like geometry with a symmetric axis at PA $\sim 23°$. Horn-like features seen in its position-velocity diagram suggest the presence of outflows close to the source (Bains et al. 2003). A relative absence of OH masers is observed in its polar regions, compared with the strong emission detected near its equator (also seen in M 1–92). This fact suggests that these areas may have been excavated by fast outflows creating empty symmetric lobes of gas (Sánchez Contreras et al. 2007). Although our HIFI observations for this source are relatively noisy (Fig. A.6), for CO $J = 9$–8, they reveal in a feature around 40 km s^{-1} expanding at $\sim$10 km s^{-1}.

3.8. R Sct

R Sct (HR 7066, HIP 92202) is a peculiar RV Tau variable whose evolutionary stage is still under debate. It presents a complex profile in all CO lines (Fig A.7). In the low-J transition $J = 2$–1, we observe a narrow double peak, which is a characteristic property of rotating disks (Bujarrabal et al. 2013). A strong blue wing is seen at these low energy levels, but as J increases, the emission of this feature is abated, suggesting a low temperature for the approaching outflow. Within our sample, this source is the one exhibiting the narrowest line profile ($\sim$10 km s^{-1}).

3.9. 89 Her

89 Her (HR 6685) is a low-mass pPN. It is a close binary system known to present a remarkable near-infrared excess due to the emission of hot dust at $\sim$1000 K (Waters et al. 1993; de Ruyter et al. 2006) and a clear far-infrared excess suggesting the presence of large grains in its dusty envelope (Shenton et al. 1995). In the $J = 2$–1 and $J = 1$–0 CO lines presented in Fig. A.8, we observe sharp profiles with a prominent central peak and weak wings at low velocities. At higher J, the structure of the profile does not change, yet their emission becomes weaker and approaches the noise level, while the wings are practically undetectable. According to its CO maps (Bujarrabal et al. 2007, 2013), this profile corresponds to a compact and unresolved component in the centre of the nebula which is suspected to be a rotating disk and an hourglass-like extended outflow (with a maximum velocity of $\sim$7 km s^{-1}).

3.10. NGC 6537

The Red Spider nebula is one of the PNe with the highest excitation known thus far (Ashley & Hyland 1988). Its spider morphology is mainly observed in the atomic emission lines, but it can also be seen in molecular hydrogen. NGC 6537 is hourglass-like and possibly multi-polar in its nebular shape (Cuesta et al. 1995). Because this PN is relatively young (its age is estimated to be $\sim$1600 yr, Matsuura et al. 2005), it has been suggested that the remnant molecular gas has not yet been accelerated enough in the polar outflows (Edwards et al. 2014). In Fig. A.9, we observe that the strong blue wing, seen as a left peak in $J = 2$–1 and $J = 1$–0 lines, decreases with J, suggesting a low temperature in the approaching outflow. There is an important interstellar medium contamination between 20 and $\sim$45 km s^{-1} in the two lowest-J CO lines, which we have tried to avoid in our study.

Table 3. Observed sources.

Source	α (J2000)	δ (J2000)	Type	SpT	d (kpc)	L ($10^3\,L_\odot$)	v_{sys} (km s^{-1})	$\dot{M}$ ($M_\odot$ yr^{-1})	Morph.	Refs.
pPNe										
IRAS 07134+1005	07 16 10.258	+09 59 47.99	C	F5Iab	3	13.5	72	5×10^{-5}	b	1, 2
IRAS 19500–1709	19 52 52.701	−17 01 50.30	C	F2-6	1	1.5	25	–	–	1
IRAS 21282+5050	21 29 58.420	+51 03 59.80	C	09.5, WC11	3	5.3	14	6×10^{-5}	–	1, 2
IRAS 22272+5435	22 29 10.374	+54 51 06.35	C	G5Ia	1.7	8.3	−28	2×10^{-5}	s	1
M 1–92	19 36 18.910	+29 32 50.00	O	B0.5IV	2.5	10	−1	2.2×10^{-4}	b	1, 3
M 2–56	23 56 36.400	+70 48 18.20	–	Be	3	10	−27	2.3×10^{-5}	b	1
OH 17.7–2.0	08 30 31.000	−14 28 57.00	O	F0	2	2.9	61	1×10^{-4}	b	1, 4
R Sct [(†)]	18 47 28.950	−05 42 18.53	O	G0-K2	0.4	4	56	3.3×10^{-7}	–	1
89 Her [(†)]	17 55 25.189	+26 02 59.97	O	F2Ibe	0.6	3.3	−8	4×10^{-6}	b	1, 5
Compact PNe										
NGC 6537	18 05 13.104	−19 50 34.88	O [(*)]	–	1.6	2	8.6	1×10^{-7}	b	6, 7, 8
M 1–16	07 37 18.955	−09 38 49.67	O	–	1.8	0.12	50	2×10^{-5}	e	2
M 1–17	07 40 22.206	−11 32 29.81	–	–	5.8	–	28	–	c	9, 10
M 3–28	18 32 41.288	−10 05 50.03	C	–	2.5	–	32	–	q	6, 11
Extended PNe										
NGC 2346	07 09 22.521	−00 48 23.60	–	A5V	0.9	–	2	–	b	6
NGC 6072	16 12 58.079	−36 13 46.06	–	B	1.39	0.39	15	–	b	6
NGC 6720	18 53 35.079	+33 01 45.03	O	hgO(H)	0.7	1	−4	2×10^{-4}	b	6, 2
NGC 6781	19 18 28.085	+06 32 19.29	C	DAO	0.95	0.35	17	–	e	6
NGC 7293	22 29 38.550	−20 50 13.60	C	DAO.5	0.22	0.09	−24	1×10^{-4}	b	6, 2

Notes. [(†)]Bipolar nebula with rotational disk. [(*)]Edwards & Ziurys (2013) questioned how O-rich NGC 6537 is. Morph. abbreviations: b: bipolar or hourglass-like, c:compact, e: elliptical, q: quadrupolar, s: spherical.
References. (1): Bujarrabal et al. (2001); (2): Fong et al. (2006); (3): Bujarrabal et al. (1998); (4): Bujarrabal et al. (1994); (5): Alcolea & Bujarrabal (1995); (6): Frew (2008); (7): Cuesta et al. (1995); (8): Edwards & Ziurys (2013); (9): Maciel (1984); (10): Bachiller et al. (1991); (11): Ziurys et al. (2020).

The same tendency is seen in $J = 6$–5 and $J = 4$–3 lines presented in Edwards et al. (2014).

Although the FIR emission of this source fills the HIFI beam for the $J = 5$–4 line entirely and exceeds it for the other lines, we considered it as a compact PN because we pointed at its centre and not their external velocity components, in contrast with what was carried out for the extended PNe. However, the fact that the lines do not come from an area smaller than the HIFI beams prevent us from performing accurate comparisons with the other compact objects and theoretical models (see Sect. 4).

3.11. M 1–16

M 1–16 is a young, compact planetary nebula known to exhibit multiple outflows with different velocities. It presents a slow outflow (with an expansion velocity of 19 km s^{-1}), which exhibits an elliptical structure and high-velocity flows consisting of three bipolar jets with shock velocities of ∼300 km s^{-1}. These fast outflows have excavated extended bipolar cavities producing symmetric lobes of molecular gas (Huggins et al. 2000). The most remarkable characteristics seen in our observed lines presented in Fig. A.10 are the extended and strong wings, indicative of high-velocity outflows and their decreasing contribution with the increase of the excitation, leaving a peak with a broad but weak pedestal in $J = 9$–8.

3.12. M 1–17

M 1–17 is a compact planetary nebula whose emission is weak at practically all wavelengths, except at the observed CO lines. Bachiller et al. (1991) studied this source in $J = 2$–1 and $J = 1$–0 and identified two components in its profile: a slow wind, with a double-peaked profile extending over 34 km s^{-1} and a fast wind, with a triangular-shape profile extending over 78 km s^{-1}. Our observations at intermediate-energy transitions (Fig. A.11) provide additional information about the molecular content of this nebula and reveal in particular a new component further away from the systemic velocity, expanding over less than 5 km s^{-1}. As the energy increases, the medium-velocity components known so far lose intensity and the component in the outskirts kicks in, indicating a higher temperature in the latter and hinting towards a possible acceleration gradient.

3.13. M 3–28

M 3–28 is a small PN, with a bipolar, butterfly-like morphology and a filamentary structure (Calvet & Cohen 1978). As shown in Fig. A.12, the line profile is relatively broad, but its exact extent at the red end cannot be accurately assessed because of the strong interstellar medium contamination that is especially visible in the low excitation lines. Our observation at higher J, however, allows us to appreciate, for the first time, the full breadth of the profile, which spans nearly 80 km s^{-1} overall. This line contamination was taken into account when selecting the velocity ranges of interest for this study (see Sect. 4.1). Apart from that, the global profile is that of a double peak on either side of a weak line core, similar to that observed in other sources, such as M 1–17 or IRAS 21282+5050.

3.14. NGC 2346

NGC 2346 is an extended bipolar PN. It has an hourglass-like geometry consisting of two open bipolar lobes and an expanding toroidal structure in its centre. This equatorial torus consists of large amounts of molecular gas and dust, and it is tilted 56° with respect to the plane of the sky (Su et al. 2004). The source is extended compared to the beams of our observations (see Fig. B.20) and the targeted region corresponds to an edge of this toroidal structure. Because, in terms of size, the CO $J = 2$–1 beam is smaller than the others, our profile consists of just one feature at the systemic velocity of the nebula. In contrast, in the other CO lines, we observe four features corresponding to four different velocity components (Fig A.13). Their emission drastically decreases at high-energy transitions, suggesting a low temperature in all these components.

3.15. NGC 6072

Near-infrared and molecular hydrogen images (Kwok et al. 2010) have characterised NGC 6072 as having an elliptical, equatorial ring and three pairs of lobes, indicating a multipolar structure. This morphology is the result of fast outflows interacting with the slow winds of the AGB phase and whose orientation is changing over time. Most of our observed CO lines present a double-peaked profile, indicative of a detached molecular shell expanding at $\sim$15 km s^{-1} (Fig. A.14). However, the emission is fully extinguished in the CO $J = 14$–13 line, suggesting a low temperature in this expanding shell.

3.16. NGC 6720

The Ring Nebula is an extended, O-rich planetary nebula with a bipolar morphology tilted with respect to the line of sight (Kwok et al. 2008; O'Dell et al. 2013). Observations of CO $J = 2$–1 and $J = 1$–0 lines carried out by Bachiller et al. (1989) and presented in Fig. 2 revealed unusually-high-velocity molecular gas. Owing, most likely, to the larger size of the CO $J = 5$–4 beam in our HIFI observations, we detected two more velocity components at roughly $\sim$15 km s^{-1} on either side of the systemic velocity. The fact that the emission of all of these components remains visible in the CO $J = 9$–8 line suggests high-temperature molecular gas at the outskirts of this nebula.

3.17. NGC 6781

NGC 6781 has an elliptical morphology very similar to that of the Ring nebula. High-resolution mapping of CO $J = 2$–1 and $J = 1$–0 lines by Bachiller et al. (1993) has provided a detailed kinematic structure of its envelope. A model, consisting of a thin, expanding, ellipsoidal shell, truncated at the two ends, was proposed by the authors to explain the observation. As we can see in Fig. A.15, our line profiles are very complex, revealing a clumpy nature for the CO shell.

3.18. NGC 7293

The Helix nebula is the closest planetary nebula of our sample. It presents an extreme bipolar morphology tilted with respect to the line of sight and a central toroidal ring. This last feature expands around the ionized nebula with arcs and filaments at high latitudes (Meaburn et al. 2005; Zeigler et al. 2013). The edge of one of these filaments corresponds to the position we have observed in this work, at offset (−435″, 75″) from the central star (Fig. B.25). As can be seen in Fig. A.16, the profile reveals various features that we treat as separate velocity components resolved along the line of sight. Their relative intensity remains constant, except in the CO $J = 9$–8 line, where their emission drops drastically, indicating that none of the observed components exhibits a high temperature. This observation suggests that most of the molecular gas of the PN has not recently been ejected, an assumption that is also supported by the findings of Zack & Ziurys (2013) and Schmidt et al. (2018).

4. Analysis and discussion

4.1. Characteristic intensities

The different velocity components evidenced in our high-resolution profiles of the CO lines provide detailed information about the excitation condition in the outflows of our objects. In particular, the relative strength of the respective spectral components and their evolution with J can vary significantly between the various sources and we use this signature here as a proxy of the evolutionary state of the nebula.

For this, we follow the method presented in Bujarrabal et al. (2012), where the contribution of each line component is estimated through its characteristic intensity over a selected velocity range in the relevant CO transition. We note beforehand that the physical meaning of the selected velocity ranges is different depending on the relative size of our objects with respect to the diameter of the instrument beams (for the record, the applicable beam sizes are collected in Table 2 and plotted on their optical and FIR images in Appendix B). In the case of compact objects, we interpret the velocity components as those of a central line core associated with the remnant of the slow AGB wind, bracketed by two (blue and red) line wings, assumed to come from the fast outflows resulting from the post-AGB axial acceleration. For two specific sources (M 1–92 and M 1–17), we also considered additional intermediate velocity ranges, that we analyse in Sect. 4.4. In the case of sources spatially resolved in most of the probed CO line (thereafter, 'extended' sources), we interpret the various features in their profiles as different velocity components probed along the line of sight crossing the nebular gas, mostly in their outskirts.

In order to define the respective velocity ranges in a systematic and objective fashion, we have taken into account the information provided in the low-J transition of CO, the systemic velocity assumed for the object, and the spatial distribution of the CO emission available, and for the extended sources, in particular. We followed a systematic procedure consisting of the selection of the velocity range of the central core that is consistent with the systemic velocity of the source. The width of the velocity component was chosen as a compromise between a sufficient number of spectral channels compared to the noise level and line ranges being sufficiently separated to avoid too much mixing between the gas probed in the respective regions. The same width was then applied to the regions associated to the red and blue wings. Overall, this leads to red and blue regions being relatively symmetrical on either side of the central core. For the narrowest profiles, the requirement to separate the envelope regions probed in each component is hard to fulfil, but we checked that small adjustments up and down the chosen widths do not impact the conclusions derived in this paper. In the case of M 3–28, the strong interstellar medium contamination, which is especially visible in the lower-J transitions was taken into account to adjust the position of the red wing, avoiding that it would fall

too close to this contribution. M 1–17 and M 1–92, additional velocity regions were considered, as explained in Sect. 4.4.

For the extended source sample, the various features are interpreted as separate velocity components along the line of sight. For this reason, the selection essentially considered the three main lines contributing to the observed profiles. The strategy regarding the choice of the velocity region width was the same as for the compact sources. In all cases, except for NGC 7293, one of the components is centred exactly on the assumed systemic velocity. In NGC 7293, the systemic velocity of $-24\,\mathrm{km\,s^{-1}}$ does not match well with the blue-shifted peak observed in the higher spectral resolution profile obtained for $J = 2$–1 and above. The velocity corresponding to this peak ($-21.7\,\mathrm{km\,s^{-1}}$) was, therefore, assigned instead to one of the components in this source. In all cases, the choice of the other two components was guided by the other line peak intensities observed in the line profile, implying that they did not necessarily fall on either side of the component selected at the systemic velocity.

The adopted velocity ranges and their characteristic intensities are compiled, alongside their corresponding 1-σ noise uncertainties, in Table 4 (compact objects) and Table 5 (extended objects). In addition, the green, blue, and red coloured intervals drawn in Figs. A.1–A.16 denote the selected regions.

4.2. Pseudo colour-colour diagrams

The relative contribution of the respective low-to-intermediate excitation CO lines can be explored by mean of the corresponding line ratio, distinctively formed for the various velocity intervals defined in the previous section. In this study, we define $R_{54/21}$ and $R_{98/54}$ as the respective ratio of the $J = 5$–4/$J = 2$–1 and $J = 9$–8/$J = 5$–4 characteristic intensities derived previously. Their uncertainties were calculated using standard error propagation, assuming absolute calibration errors of 20% for $J = 2$–1, and 15% for $J = 5$–4 and $J = 9$–8 (HIFI Handbook[1]). As explained in Sect. 4.1, the physical meaning of the chosen velocity interval is different for the compact and extended sources in our sample. This distinction also has implications in the analysis of the ratios discussed here. For compact sources, we distinguish the ratios computed over the line core intervals and those computed over the line wings intervals – for the latter, we take an average of both the red and blue wings. For extended sources, the ratios are computed for each separate velocity component, as well as based on the averaged intensities over all considered components. These respective ratios are compiled in Table 4 (compact sources) and Table 5 (extended sources).

We then plot the $R_{98/54}$ ratio against the $R_{54/21}$ one, which we call in the following pseudo colour-colour diagrams (thereafter cc-diagram). Although different CO transitions were probed by Bujarrabal et al. (2012), we decided to also represent in this diagram the ratios obtained for five sources (CRL 2688, CRL 618, IRAS 07134+1005, OH 231.8+4.2 and NGC 6302) by replacing the $J = 5$–4 line by the $J = 6$–5 one, and the $J = 9$–8 line by the $J = 10$–9 one. While not strictly comparable to our own ratios, we added those points to check the general trends in the pseudo colour-colour space.

Figure 3 shows this diagram for the wings of the compact sources, and the intensity averages of the extended objects. Three different groups emerge from this plot: extended planetary nebulae, compact planetary nebulae and protoplanetary nebulae. Extended planetary nebulae (in black) all show low values of the average $R_{98/54}$ ratio (typically below unity), while their $R_{54/21}$ ratio spreads over an interval range from 0.16 to 0.9. Compact planetary nebulae (in blue), however, seem to concentrate low values of $R_{54/21}$ (all below 0.2), while their $R_{98/54}$ ratio is typically between 0.5 and 1, with the exception of NGC 6537 (see discussion later in this paper). Protoplanetary nebulae (in orange) also show a relatively low $R_{54/21}$ ratio (around 0.1 on average), but their $R_{98/54}$ ratio, on the other hand, takes values that are systematically in excess of unity.

Although they are not strictly based on the same metrics, the sources from Bujarrabal et al. (2012) follow this general classification, but with a certain deviation. On the one hand, CRL 618 shows a noticeably higher $R_{65/21}$ ratio (i.e. around 0.4), while OH 231.8+4.2 only offers an upper limit to the $R_{109/65}$ ratio located well below 1. Still, the younger objects are mainly located in the upper left corner of the diagram, while the planetary nebulae tend to be in the lower area.

The overall trends observed in Fig. 3 suggest that $R_{98/54}$ (and the equivalent ratio formed from the $J = 10$–9 over $J = 6$–5 ratio for the sources in Bujarrabal et al. 2012) is sensitive to the evolutionary stage of the nebulae. This manifests as a higher excitation state in the high-velocity gas of pPNe than in the shocked gas probed in the PNe. NGC 6537 stands as a noticeable exception in that respect. Although considered a compact planetary nebula in our sample, the optical and FIR maps (Fig. B.13) indicates that the source is partially resolved within the HIFI beam for the $J = 5$–4 transition. Moreover, if the different features we see are interpreted as separate velocity components, their observational characteristics differ from those in the rest of the extended object sample, as the spectra were collected very close to the source photocentre (while most lines-of-sight in the extended source sample pointed towards offset regions of the nebula). As such, NGC 6537 is not directly comparable to either of the compact or extended PN source samples and this fact could explain its outlying location on the diagram.

We also note that the wings of 89 Her, R Sct, OH 17.7–2.0 and M 2–56 are not detected at high-J (they are not featured in Fig. 3, but their ratios in the line core are shown in Fig. 4). As we mentioned in Sect. 3, 89 Her and R Sct are considered bipolar nebulae with a rotational disk. It is believed that this type of nebula concentrates all its gas in the disk and central region and, as such, they are considered compact objects suffering from severe dilution in the beam of the telescope.

A comparison of the line ratios as measured in the line wings and line core of the compact objects is shown in Fig. 4. Each pair of ratios is joined with an arrow pointing toward the line cores, allowing us to trace possible trends between the relative excitation of the outflows with regard to that of the cores. We note that the arrows of the pPNe sub-sample have greater amplitude and point downwards, indicating that the temperature of their fast outflows must be higher than in the slow winds and suggesting, therefore, a more recent gas acceleration. On the contrary, the difference between the ratios in the line wings and the line cores of the compact PNe sub-sample is smaller and most of their arrows point upwards, indicative of cooler and older gas in the fast flows. This trend is similar to that reported in Bujarrabal et al. (2012) for the objects of their sample represented in our pseudo colour-colour diagram.

Figure 4 also includes a visualisation of the distribution of the line ratios for the various components of the extended PNe sub-samples. In this case, the ratio in each component is connected to that of the averaged ratios shown in Fig. 3.

[1] https://www.cosmos.esa.int/web/herschel/legacy-documentation-hifi

Table 4. Characteristic intensities of the three representative features identified in the CO profiles of the compact objects, and their corresponding coordinates in the pseudo cc-diagram presented in Figs. 3 and 4.

Source	^{12}CO line	Observation ID	Central core average T_{mb}(K)	Blue wing av. T_{mb}(K)	Red wing av. T_{mb}(K)	Noise rms (K)	Line ratios Central core	Line ratios Averaged line wings
LSR velocity ranges (km s^{-1})			69.5 – 74.5	61.5 – 66.5	77.5 – 82.5			
IRAS 07134+1005	J = 1–0		1.32	0.54	1.05	0.05	$R_{54/21} = 0.13$	$R_{54/21} = 0.15$
	J = 2–1		2.05	0.48	1.22	0.04		
	J = 5–4	1342244408	0.263	0.090	0.134	0.004	$R_{98/54} = 1.07$	$R_{98/54} = 2.05$
	J = 9–8	1342229927	0.281	0.236	0.200	0.004		
LSR velocity ranges (km s^{-1})			19.5 – 29.5	1 – 11	40 – 50			
IRAS 19500–1709	J = 1–0		0.83	0.15	0.06	0.01		
	J = 2–1		2.06	0.62	0.35	0.01	$R_{54/21} = 0.05$	$R_{54/21} = 0.11$
	J = 5–4	1342216805	0.104	0.068	0.036	0.003		
	J = 9–8	1342216811	0.224	0.162	0.076	0.003	$R_{98/54} = 2.16$	$R_{98/54} = 2.24$
	J = 14–13	1342231774	0.13	0.09	0.05	0.01		
LSR velocity ranges (km s^{-1})			11.9 – 19.9	2.5 – 10.5	22 – 30			
IRAS 21282+5050	J = 1–0		1.21	0.52	1.05	0.01		
	J = 2–1		2.30	0.78	1.99	0.02	$R_{54/21} = 0.28$	$R_{54/21} = 0.30$
	J = 5–4	1342200921	0.653	0.199	0.704	0.004		
	J = 9–8	1342210667	0.626	0.522	1.054	0.004	$R_{98/54} = 0.96$	$R_{98/54} = 2.06$
	J = 14–13	1342220506	0.42	0.57	0.78	0.01		
LSR velocity ranges (km s^{-1})			−30.5 – −25.5	−37.3 – −32.3	−23.2 – −18.2			
IRAS 22272+5435	J = 1–0		3.14	2.03	1.69	0.02	$R_{54/21} = 0.034$	$R_{54/21} = 0.03$
	J = 2–1		8.76	3.69	3.45	0.02		
	J = 5–4	1342200922	0.294	0.120	0.115	0.004	$R_{98/54} = 1.52$	$R_{98/54} = 2.12$
	J = 9–8	1342213360	0.448	0.253	0.245	0.004		
LSR velocity ranges (km s^{-1})			−7.5 – 7.5	−41.5 – −26.5	26.5 – 41.5			
M 1–92	J = 1–0		0.60	0.16	0.20	0.01	$R_{54/21} = 0.059$	$R_{54/21} = 0.08$
	J = 2–1		1.48	0.29	0.55	0.02		
	J = 5–4	1342210076	0.087	0.032	0.030	0.003	$R_{98/54} = 0.51$	$R_{98/54} = 1.64$
	J = 9–8	1342220500	0.045	0.045	0.055	0.002		
LSR velocity ranges (km s^{-1})			−29 – −13	−52 – −36	5 – 21			
M 2–56	J = 1–0		0.181	0.152	0.058	0.003	$R_{54/21} = 0.07$	–
	J = 2–1		0.86	0.82	0.28	0.01		
	J = 5–4	1342201534	0.058	0.067	$\lesssim$0.005	0.003	$R_{98/54} \lesssim 0.08$	–
	J = 9–8	1342213359	$\lesssim$0.005	$\lesssim$0.005	$\lesssim$0.005	0.002		
LSR velocity ranges (km s^{-1})			59.5 – 64.5	49.5 – 54.5	69.5 – 74.5			
OH 17.7–2.0	J = 1–0		1.48	1.13	0.84	0.07	$R_{54/21} \lesssim 0.01$	–
	J = 2–1		0.98	0.48	0.44	0.05		
	J = 5–4	1342218429	$\lesssim$0.009	$\lesssim$0.009	$\lesssim$0.009	0.005	–	–
	J = 9–8	1342228622	0.064	$\lesssim$0.008	$\lesssim$0.008	0.004		
LSR velocity ranges (km s^{-1})			54.5 – 56.5	51 – 53	57.2 – 59.2			
R Sct	J = 1–0		0.91	0.57	0.91	0.03	$R_{54/21} = 0.05$	–
	J = 2–1		1.48	0.53	1.36	0.02		
	J = 5–4	1342230387	0.069	$\lesssim$0.012	0.044	0.006	$R_{98/54} \lesssim 0.16$	–
	J = 9–8	1342229922	$\lesssim$0.011	$\lesssim$0.011	$\lesssim$0.011	0.005		
LSR velocity ranges (km s^{-1})			−10 – −6	−15.5 – −11.5	−5 – −1			
89 Her	J = 1–0		0.62	0.2	0.18	0.01	$R_{54/21} = 0.03$	–
	J = 2–1		1.36	0.44	0.30	0.01		
	J = 5–4	1342214335	0.043	$\lesssim$0.010	$\lesssim$0.010	0.005	$R_{98/54} = 0.71$	–
	J = 9–8	1342218624	0.030	$\lesssim$0.009	$\lesssim$0.009	0.005		
LSR velocity ranges (km s^{-1})			5.5 – 10.5	−0.5 – 4.5	11.5 – 16.5			
NGC 6537	J = 1–0		1.72	1.04	1.09	0.03		
	J = 2–1		3.48	2.51	1.88	0.05	$R_{54/21} = 0.14$	$R_{54/21} = 0.12$
	J = 5–4	1342217693	0.471	0.211	0.296	0.004		
	J = 9–8	1342215913	0.917	0.286	0.608	0.004	$R_{98/54} = 1.95$	$R_{98/54} = 1.7$
	J = 14–13	1342229785	0.94	0.20	0.62	0.01		
LSR velocity ranges (km s^{-1})			45.8 – 54.2	35.8 – 44.2	55.8 – 64.2			
M 1–16	J = 1–0		1.58	1.43	1.61	0.02	$R_{54/21} = 0.07$	$R_{54/21} = 0.06$
	J = 2–1		3.91	3.24	3.74	0.03		
	J = 5–4	1342220515	0.271	0.237	0.210	0.003	$R_{98/54} = 0.65$	$R_{98/54} = 0.40$
	J = 9–8	1342220495	0.176	0.083	0.097	0.003		
LSR velocity ranges (km s^{-1})			25 – 31	3.5 – 9.5	47 – 53			
M 1–17	J = 1–0		1.16	0.09	0.13	0.03	$R_{54/21} = 0.06$	$R_{54/21} = 0.13$
	J = 2–1		1.93	0.54	0.37	0.04		
	J = 5–4	1342218900	0.113	0.058	0.056	0.005	$R_{98/54} = 1.02$	$R_{98/54} = 0.80$
	J = 9–8	1342220494	0.115	0.053	0.038	0.004		
LSR velocity ranges (km s^{-1})			29.5 – 34.5	15.5 – 20.5	41.5 – 46.5			
M 3–28	J = 1–0		1.93	2.99	3.09	0.02	$R_{54/21} = 0.11$	$R_{54/21} = 0.10$
	J = 2–1		2.61	4.22	4.90	0.04		
	J = 5–4	1342218430	0.289	0.412	0.474	0.006	$R_{98/54} = 0.47$	$R_{98/54} = 0.48$
	J = 9–8	1342218214	0.136	0.174	0.257	0.004		

Table 5. Characteristic intensities of the identified velocity components and the coordinates of the CO profiles of extended sources in the pseudo cc-diagram shown in Fig. 3.

Source	^{12}CO line	Observation ID	Component #1 average T_{mb}(K)	Component #2 av. T_{mb}(K)	Component #3 av. T_{mb}(K)	Noise rms (K)	Averaged line ratio of all components
LSR velocity ranges (km s^{-1})			12 – 17	−0.5 – 4.5	21.5 – 26.5		
NGC 2346	J = 1–0		0.76	0.12	0.17	0.04	$R_{54/21} = 0.27$
	J = 2–1		1.75	0.07	0.09	0.02	
	J = 5–4	1342218901	0.400	0.069	0.142	0.003	$R_{98/54} \lesssim 0.06$
	J = 9–8	1342229928	0.061	$\lesssim$0.007	$\lesssim$0.007	0.004	
LSR velocity ranges (km s^{-1})			11 – 19	−6 – 2	25 – 33		
NGC 6072	J = 1–0		0.39	0.31	0.35	0.04	
	J = 2–1		0.61	0.29	0.82	0.02	$R_{54/21} = 0.87$
	J = 5–4	1342213733	0.859	0.154	0.980	0.003	
	J = 9–8	1342216328	0.150	$\lesssim$0.006	0.293	0.003	$R_{98/54} = 0.24$
	J = 14–13	1342229786	$\lesssim$0.02	$\lesssim$0.02	$\lesssim$0.02	0.01	
LSR velocity ranges (km s^{-1})			−7 – −1	−19 – −13	13 – 19		
NGC 6720	J = 1–0		0.18	0.30	$\lesssim$0.04	0.02	$R_{54/21} = 0.26$
	J = 2–1		0.36	1.57	$\lesssim$0.06	0.03	
	J = 5–4	1342210075	0.207	0.323	0.127	0.004	$R_{98/54} = 0.33$
	J = 9–8	1342220499	0.076	0.084	$\lesssim$0.007	0.003	
LSR velocity ranges (km s^{-1})			13 – 21	−4.4 – 3.6	25.8 – 33.8		
NGC 6781	J = 1–0		0.46	0.90	0.19	0.06	$R_{54/21} = 0.36$
	J = 2–1		1.43	2.60	$\lesssim$0.14	0.07	
	J = 5–4	1342230381	0.435	0.631	0.332	0.003	$R_{98/54} = 0.12$
	J = 9–8	1342229920	0.049	0.098	$\lesssim$0.006	0.003	
LSR velocity ranges (km s^{-1})			−18.5 – −15.5	−23.2 – −20.2	−15 – −12		
NGC 7293	J = 1–0		1.99	1.45	1.75	0.11	$R_{54/21} = 0.16$
	J = 2–1		1.65	0.97	1.07	0.01	
	J = 5–4	1342210082	0.265	0.131	0.251	0.004	$R_{98/54} \lesssim 0.06$
	J = 9–8	1342220502	$\lesssim$0.007	$\lesssim$0.007	$\lesssim$0.007	0.004	

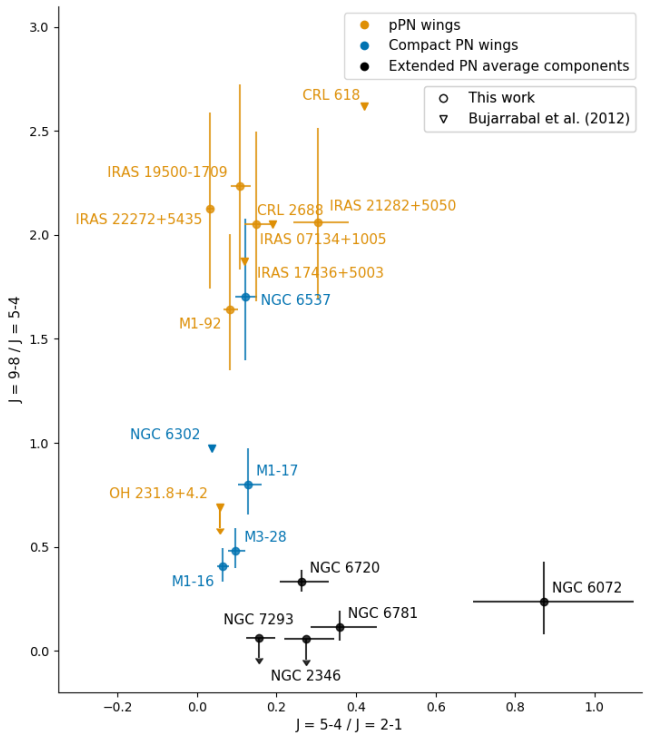


Fig. 3. Pseudo colour-colour diagram comparing the $J = 5–4/J = 2–1$ and $J = 9–8/J = 5–4$ intensity ratios of the wings for the compact sources and the line profiles for the extended PNe. Although they are based on different line ratios, some sources from Bujarrabal et al. (2012) are also included here (see text for details).

At most, this should indicate whether the individual velocity components in each object do or do not share certain conditions of excitation or evolution. Overall, there is no clear trend derived from them. In the case of NGC 6781, all three components seem to behave similarly, while NGC 2346, for example, exhibits a larger spread of physical conditions in the line ratios.

4.3. Comparison with theoretical predictions

We compare in this section the distribution of our line ratios with theoretical predictions in order to estimate the physical conditions in the fast outflows of our source sample. To this aim, we have performed simplified calculation based on the large velocity gradient (LVG) approximation, for a grid of density, $n_{\rm tot}$, and kinetic temperature, $T_{\rm k}$, as well as different optical depth regimes. This assumption is justified by the kinematics at play in pPNe and many PNe. We also assume that no strong radiative interactions take place between distant points of the envelope exhibiting very different physical conditions. The code is similar to the one used by Bujarrabal et al. (2012); we have updated the calculation of the collisional transition probabilities, including, in particular, a more accurate interpolation between rates for different temperatures and allowing for calculations at a higher number of levels.

Our computations are based on canonical envelope properties assuming the following parameters: a distance to the central star of $R = 6 \times 10^{16}$ cm, an expansion velocity of $V_{\rm exp} = 15$ km s^{-1} and a relative abundance of $X(^{12}{\rm CO}) = 2 \times 10^{-4}$ (for more details, see Sect. 3.1. of Bujarrabal et al. 2012). Opacity effects are taken into account in the calculations under the usual assumptions of the LVG approximation. Although such an assumption implies a constant value for $R\,X/V_{\rm exp}$ (where $n_{\rm tot} R\,X/V_{\rm exp}$ represents the column density opacity under the LVG approximation), this approach offers an empirical set of models which is sufficient to probe the statistical behaviour of

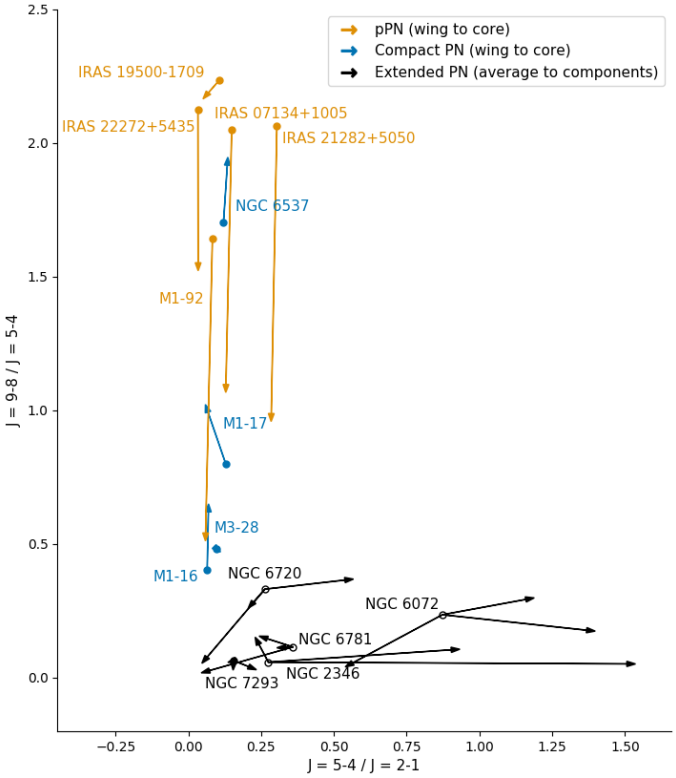


Fig. 4. Pseudo colour-colour diagram comparing the $J = 5$–$4/J = 2$–1 and $J = 9$–$8/J = 5$–4 intensity ratios of the wings and cores of the compact sources (joined by arrows pointing towards the line cores) and the identified velocity components of the extended PNe (connecting ratios of each component to its average).

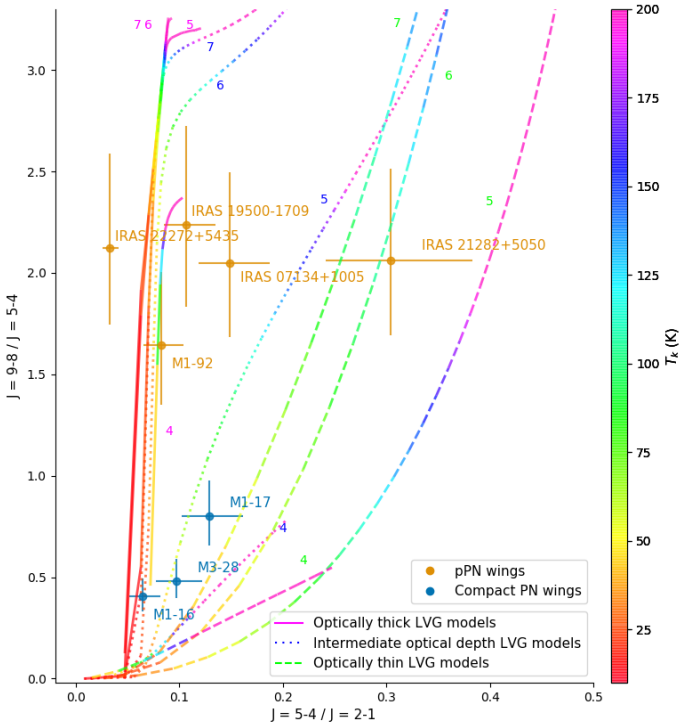


Fig. 5. Pseudo colour-colour diagram comparing the $J = 5$–$4/J = 2$–1 and $J = 9$–$8/J = 5$–4 intensity ratios of pPNe line wings, compact PNe line wings and the LVG models for different optical depths (solid, dotted and dashed lines), densities (number indicates $\log_{10}(n_{\rm tot})$) and temperatures (coded as shown in the colour scale). See text for further details.

our line ratios in this grid. Similarly, because we want to locate all our objects in the same set of model space, we do not include any ad hoc modelling of the large-scale structure of the nebula.

We also assume that the lines come from a region significantly smaller than the telescope spatial resolution, which applies to our compact source sample. For comparison with our extended nebulae, we corrected our line ratio calculations, taking into account the ratios of the applicable telescope beams (Table 2).

Figure 5 shows our predicted line ratios for several optical depths, densities, and temperature regimes within the ranges relevant to our data. The theoretical results for different temperatures are presented using a colour coding where the adopted scale ranges from 10 K to 200 K. As anticipated in Sect. 4.2, the ^{12}CO $J = 9$–$8/J = 5$–4 ratio appears as a good proxy for the kinetic temperature, especially in the optically thick regime. The slope of this relationship is also related to the density. Conversely, the ^{12}CO $J = 5$–$4/J = 2$–1 ratio appears to be inversely proportional to both optical depth and density. Unfortunately, predictions from the various model grids overlap in the pseudo colour-colour diagram, leading to some degeneracy in the derivation of the physical conditions from our measurements. Figure 5 also shows the intensity ratios of the line wings for the compact sources.

From the comparison of our pPN observational results with the LVG predictions, we observe that high density optically thick models predict too low temperatures (<25 K) for the outflows of this kind of objects, while the optically thin approximations assign densities excessively high (larger than 10^7 cm^{-3}). Consequently, we used the model grid based on an intermediate optical depth and optically thick models of 10^4 cm^{-3}, for which the fast outflows of protoplanetary nebulae are compatible with densities between 10^4 and 10^6 cm^{-3} and temperatures in the range of 75–200 K. Doing the same exercise for the compact PNe, we derive lower kinetic temperatures in the 25–75 K range and densities in the 10^4–10^6 cm^{-3} range.

We interpret this result as a relation between the temperature of the high-velocity gas found in the nebulae and the time elapsed since its acceleration due to shocks. The heated and accelerated gas reaches high temperatures during the ejection of very fast outflows, but it cools in a short period of time. This is consistent with the results already reported by Bujarrabal et al. (2012). The correlation between the density of the warm regions and the evolutionary stage of the nebulae, however, is not so clear.

4.4. Intermediate velocity ranges

Aside from the main spectral components analysed above, we note the existence of intermediate velocity features in some of our sources, particularly in M 1–92 and M 1–17. Following the same methods described in the previous sections, we derived the characteristic intensities and respective $R_{54/21}$ and $R_{98/54}$ ratios of these intermediate line regions for the two mentioned nebulae. Their values are collected in Table 6, alongside the LSR velocity ranges adopted (also marked in Figs. A.4 and A.11). The substantial difference between the ratios of these regions and those estimated in the line wings is indicative of a cooler gas component of intermediate velocity in the nebulae that, in the case of M 1–92, could correspond with the lobe walls identified in Alcolea et al. (2007) and Bujarrabal et al. (1998).

Table 6. Characteristic intensities of two intermediate velocity ranges identified in the CO profiles of the pPNe M 1–17 and M 1–92, and their derived ratios

Source	^{12}CO line	Blue interm. wing av. T_{mb}(K)	Red interm. wing av. T_{mb}(K)	Noise rms (K)	Line ratios Blue interm. line wings	Line ratios Red interm. line wings
LSR velocity ranges (km s^{-1})		−25 – −10.5	10.5 – 25			
M 1–92	J = 1–0	0.36	0.43	0.01	$R_{54/21}$ = 0.05	$R_{54/21}$ = 0.04
	J = 2–1	0.88	1.18	0.02		
	J = 5–4	0.048	0.052	0.002	$R_{98/54}$ = 0.55	$R_{98/54}$ = 0.68
	J = 9–8	0.026	0.035	0.002		
LSR velocity ranges (km s^{-1})		11.5 – 23.5	32 – 44			
M 1–17	J = 1–0	1.06	1.11	0.03	$R_{54/21}$ = 0.06	$R_{54/21}$ = 0.08
	J = 2–1	1.86	1.89	0.04		
	J = 5–4	0.112	0.144	0.005	$R_{98/54}$ = 1.19	$R_{98/54}$ = 0.94
	J = 9–8	0.133	0.135	0.004		

5. Conclusions

We used the high-resolution spectrometer HIFI on board *Herschel* to survey a sample of nine protoplanetary nebulae (pPNe) and nine planetary nebulae (PNe) in intermediate-excitation molecular lines of ^{12}CO (J = 5–4, J = 9–8, and J = 14–13 for a subset of those). We complemented these data with observations of the low-J transitions of CO using IRAM 30m telescope and literature (Table 1). The selected lines are shown in Figs. A.1–A.16 and described briefly in Sect. 3.

As in Bujarrabal et al. (2012), we carried out a simplified analysis of the CO lines in terms of the emission of three representative profile components. The physical significance behind these regions depends on the relative size of the objects with regard to the dimension of HIFI beams. Five of the PNe in our sample were considered extended sources and we interpreted their three main profile features as three different velocity components. On the other hand, the representative profile features of the compact nebulae were analysed as a line core (known to come from the remnant AGB shell and rotating disks in two cases) and two line wings (associated with the fast outflows).

In Tables 4 and 5, we compiled the averaged intensities of the characteristic components found in compact and extended sources respectively, together with their errors. These tables indicate the intensity ratios J = 5–4/J = 2–1 and J = 9–8/J = 5–4 derived for the line core and line wings of compact objects, and for the entire line profile of extended nebulae. These ratios are represented in Figs. 3 and 4 as so-called pseudo colour-colour diagrams. In these diagrams, our sample is clearly divided with regard to their evolutionary stage and to their relative extension. While the wings of pPNe are located at the top left of the diagram and are significantly more excited than their cores, the wings of PNe are found at its bottom left and are less excited than their cores. This observation suggests a correlation between the evolutionary stage of nebulae and the excitation state of their fast outflows. With respect to the apparent spatial extension, compact objects remain at the left of the pseudo cc-diagram, while the extended sources are found at its bottom right.

We performed radiative transfer calculations based on the LVG approximation to derive the physical properties of the nebular gas. We found that the kinetic temperatures of the fast gas presented in pPNe tend to be higher (with typical values between 75-200 K) than those found in PNe (with characteristic temperatures between 25 and 75 K). This result indicates a relation between the temperature of fast outflows and the time elapsed since their ejection. It is interpreted as the effect of cooling in the heated and accelerated gas during the pPN phase, when the shocks propagate across the nebula. This conclusion is strengthened by the significantly high excitation state found for the high-velocity line wings in M 1–92 (much higher than for the intermediate-velocity wings); the high-velocity emission is indeed known to come from the tips of the nebula lobes, which are directly impinged by the post-AGB jets.

Acknowledgements. We thank the anonymous referee for their useful and constructive comments on the paper. We also thank Prof. Hans Olofsson for his thorough review of this manuscript. HIFI has been designed and built by a consortium of institutes and university departments from across Europe, Canada and the USA under the leadership of SRON Netherlands Institute for Space Research, Groningen, The Netherlands, and with major contributions from Germany, France and the USA. Consortium members are: Canada: CSA, U.Waterloo; France: CESR, LAB, LERMA, IRAM; Germany: KOSMA, MPIfR, MPS; Ireland: NUI Maynooth; Italy: ASI, IFSI-INAF, Osservatorio Astrofisico di Arcetri-INAF; The Netherlands: SRON, TUD; Poland: CAMK, CBK; Spain: Observatorio Astronómico Nacional (IGN), Centro de Astrobiología (CSIC-INTA); Sweden: Chalmers University of Technology – MC2, RSS and GARD; Onsala Space Observatory; Swedish National Space Board, Stockholm University – Stockholm Observatory; Switzerland: ETH Zurich, FHNW; USA: Caltech, JPL, NHSC. This paper is based on obser-vations carried out at the IRAM-30 m single-dish telescope. IRAM is sup-ported by INSU/CNRS (France), MPG (Germany) and IGN (Spain). JA and VB are partly funded by the Spanish MICIIN grant AYA2016-78994-P.

References

Alcolea, J., & Bujarrabal, V. 1995, A&A, 303, L21
Alcolea, J., Bujarrabal, V., Sánchez Contreras, C., Neri, R., & Zweigle, J. 2001, A&A, 373, 932
Alcolea, J., Neri, R., & Bujarrabal, V. 2007, A&A, 468, L41
Ashley, M. C. B., & Hyland, A. R. 1988, ApJ, 331, 532
Bachiller, R., Bujarrabal, V., Martin-Pintado, J., & Gomez-Gonzalez, J. 1989, A&A, 218, 252
Bachiller, R., Huggins, P. J., Cox, P., & Forveille, T. 1991, A&A, 247, 525
Bachiller, R., Huggins, P. J., Cox, P., & Forveille, T. 1993, A&A, 267, 177
Bachiller, R., Forveille, T., Huggins, P. J., & Cox, P. 1997, A&A, 324, 1123
Bains, I., Gledhill, T. M., Yates, J. A., & Richards, A. M. S. 2003, MNRAS, 338, 287
Balick, B., & Frank, A. 2002, ARA&A, 40, 439
Bublitz, J., Kastner, J. H., Santander-García, M., et al. 2019, A&A, 625, A101
Bujarrabal, V., Alcolea, J., & Planesas, P. 1992, A&A, 257, 701
Bujarrabal, V., Fuente, A., & Omont, A. 1994, A&A, 285, 247
Bujarrabal, V., Alcolea, J., & Neri, R. 1998, ApJ, 504, 915
Bujarrabal, V., Castro-Carrizo, A., Alcolea, J., & Sánchez Contreras, C. 2001, A&A, 377, 868
Bujarrabal, V., van Winckel, H., Neri, R., et al. 2007, A&A, 468, L45
Bujarrabal, V., Alcolea, J., Soria-Ruiz, R., et al. 2012, A&A, 537, A8
Bujarrabal, V., Alcolea, J., Van Winckel, H., Santander-García, M., & Castro-Carrizo, A. 2013, A&A, 557, A104
Calvet, N., & Cohen, M. 1978, MNRAS, 182, 687
Castro-Carrizo, A., Bujarrabal, V., Sánchez Contreras, C., Alcolea, J., & Neri, R. 2002, A&A, 386, 633

Castro-Carrizo, A., Quintana-Lacaci, G., Neri, R., et al. 2010, A&A, 523, A59
Cox, P., Omont, A., Huggins, P. J., Bachiller, R., & Forveille, T. 1992, A&A, 266, 420
Cuesta, L., Phillips, J. P., & Mampaso, A. 1995, A&A, 304, 475
Danilovich, T., Teyssier, D., Justtanont, K., et al. 2015, A&A, 581, A60
De Beck, E., Decin, L., de Koter, A., et al. 2010, A&A, 523, A18
de Graauw, T., Helmich, F. P., Phillips, T. G., et al. 2010, A&A, 518, L6
de Ruyter, S., van Winckel, H., Maas, T., et al. 2006, A&A, 448, 641
Edwards, J. L., & Ziurys, L. M. 2013, ApJ, 770, L5
Edwards, J. L., Cox, E. G., & Ziurys, L. M. 2014, ApJ, 791, 79
Fong, D., Meixner, M., Sutton, E. C., Zalucha, A., & Welch, W. J. 2006, ApJ, 652, 1626
Frew, D. J. 2008, PhD Thesis, Department of Physics, Macquarie University, NSW 2109, Australia
Gledhill, T. M. 2005, MNRAS, 356, 883
Gledhill, T. M., Chrysostomou, A., Hough, J. H., & Yates, J. A. 2001, MNRAS, 322, 321
Heske, A., Forveille, T., Omont, A., van der Veen, W. E. C. J., & Habing, H. J. 1990, A&A, 239, 173
Hrivnak, B. J., Kwok, S., & Volk, K. M. 1989, ApJ, 346, 265
Huggins, P. J., Forveille, T., Bachiller, R., & Cox, P. 2000, ApJ, 544, 889
Justtanont, K., Barlow, M. J., Tielens, A. G. G. M., et al. 2000, A&A, 360, 1117
Kwok, S., Volk, K. M., & Hrivnak, B. J. 1989, ApJ, 345, L51
Kwok, S., Chong, S.-N., Koning, N., Hua, T., & Yan, C.-H. 2008, ApJ, 689, 219
Kwok, S., Chong, S.-N., Hsia, C.-H., Zhang, Y., & Koning, N. 2010, ApJ, 708, 93
Le Bertre, T. 1987, A&A, 180, 160
Maciel, W. J. 1984, A&AS, 55, 253
Matsuura, M., Zijlstra, A. A., Gray, M. D., Molster, F. J., & Waters, L. B. F. M. 2005, MNRAS, 363, 628
Meaburn, J., Boumis, P., López, J. A., et al. 2005, MNRAS, 360, 963
Meixner, M., Skinner, C. J., Graham, J. R., et al. 1997, Astronomy Data Image Library
Milam, S. N., Woolf, N. J., & Ziurys, L. M. 2009, ApJ, 690, 837
O'Dell, C. R., Ferland, G. J., Henney, W. J., & Peimbert, M. 2013, AJ, 145, 170
Omont, A., Moseley, S. H., Cox, P., et al. 1995, ApJ, 454, 819
Sánchez Contreras, C., Bujarrabal, V., Castro-Carrizo, A., Alcolea, J., & Sargent, A. 2004, ApJ, 617, 1142
Sánchez Contreras, C., Le Mignant, D., Sahai, R., Gil de Paz, A., & Morris, M. 2007, ApJ, 656, 1150
Schmidt, D. R., & Ziurys, L. M. 2016, ApJ, 817, 175
Schmidt, D. R., Zack, L. N., & Ziurys, L. M. 2018, ApJ, 864, L31
Shenton, M., Evans, A., & Williams, P. M. 1995, MNRAS, 273, 906
Shibata, K. M., Tamura, S., Deguchi, S., et al. 1989, ApJ, 345, L55
Su, K. Y. L., Kelly, D. M., Latter, W. B., et al. 2004, ApJS, 154, 302
Teyssier, D., Alcolea, J., Bujarrabal, V., et al. 2011, in The Molecular Universe, eds. J. Cernicharo, R. Bachiller, et al., IAU Symp., 280, 353
Ueta, T., Meixner, M., & Bobrowsky, M. 2000, ApJ, 528, 861
Van Winckel, H., & Reyniers, M. 2000, A&A, 354, 135
Waters, L. B. F. M., Waelkens, C., Mayor, M., & Trams, N. R. 1993, A&A, 269, 242
Young, K., Cox, P., Huggins, P. J., Forveille, T., & Bachiller, R. 1999, ApJ, 522, 387
Zack, L. N., & Ziurys, L. M. 2013, ApJ, 765, 112
Zeigler, N. R., Zack, L. N., Woolf, N. J., & Ziurys, L. M. 2013, ApJ, 778, 16
Zhang, Y., Kwok, S., & Dinh-V-Trung 2008, ApJ, 678, 328
Ziurys, L. M., Schmidt, D. R., & Woolf, N. J. 2020, ApJ, 900, L31

Appendix A: CO spectra of the source sample

In this section, we compile all the CO transition spectra used in this work, together with the adopted systemic velocity and velocity ranges considered in the analysis. See the captions in Figs. 1 and 2 for further details.

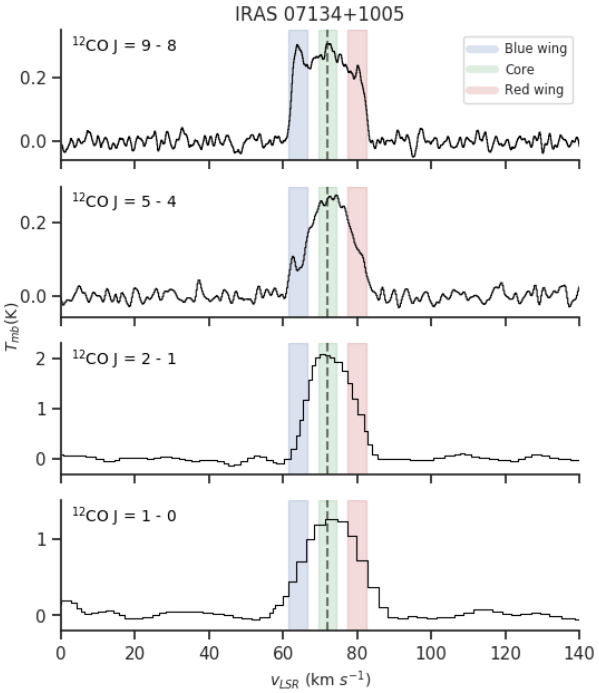


Fig. A.1. Observations of IRAS 07134+1005. Shadowed regions mark the LSR velocity ranges adopted for each feature and the dashed vertical line indicates the systemic velocity.

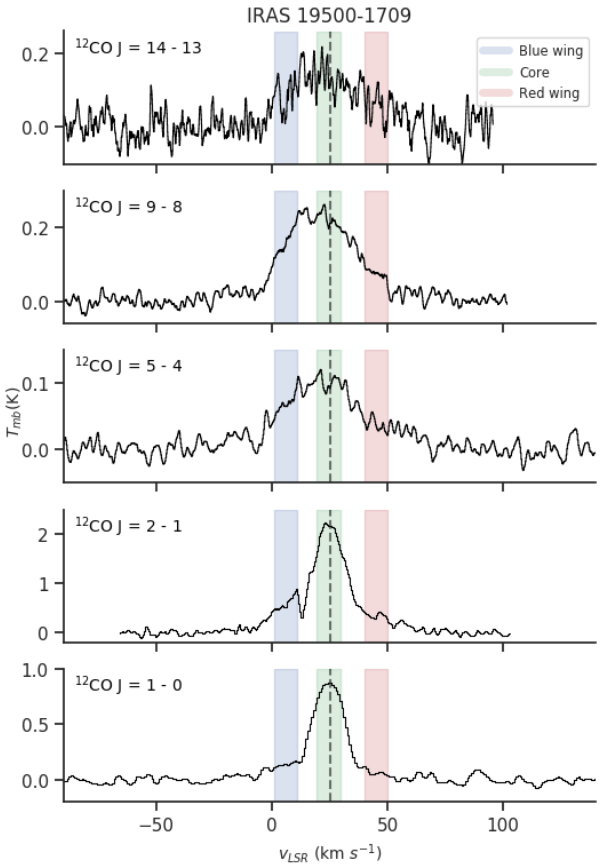


Fig. A.2. Observations of IRAS 19500–1709. Shadowed regions mark the LSR velocity ranges adopted for each feature and the dashed vertical line indicates the systemic velocity.

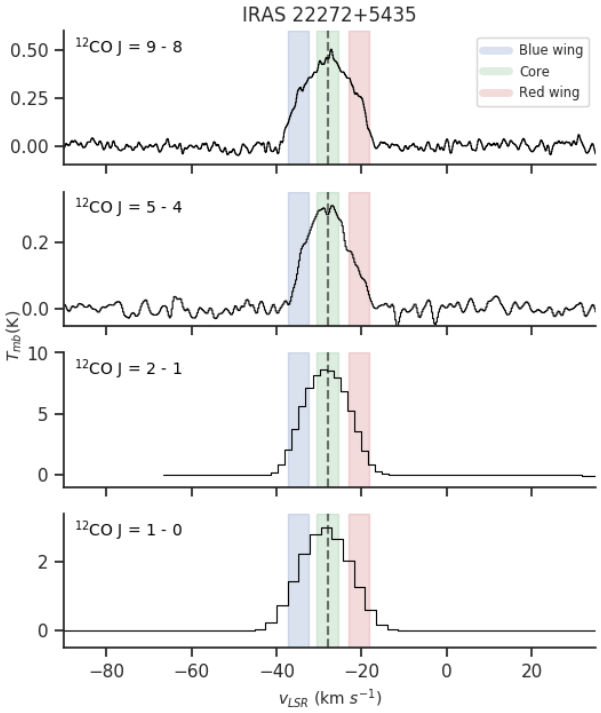


Fig. A.3. Observations of IRAS 22272+5435. Shadowed regions mark the LSR velocity ranges adopted for each feature and the dashed vertical line indicates the systemic velocity.

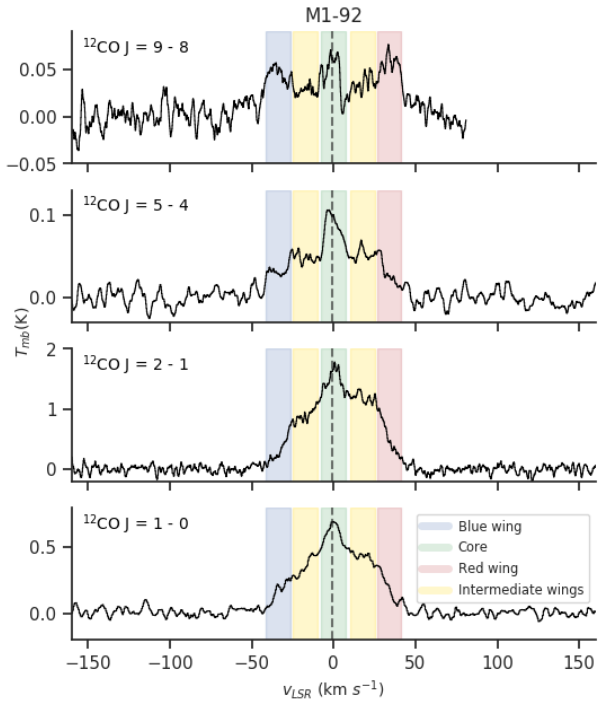


Fig. A.4. Observations of M 1–92. Shadowed regions mark the LSR velocity ranges adopted for each feature and the dashed vertical line indicates the systemic velocity. See Sect. 4.4 for the reference to the intermediate wings.

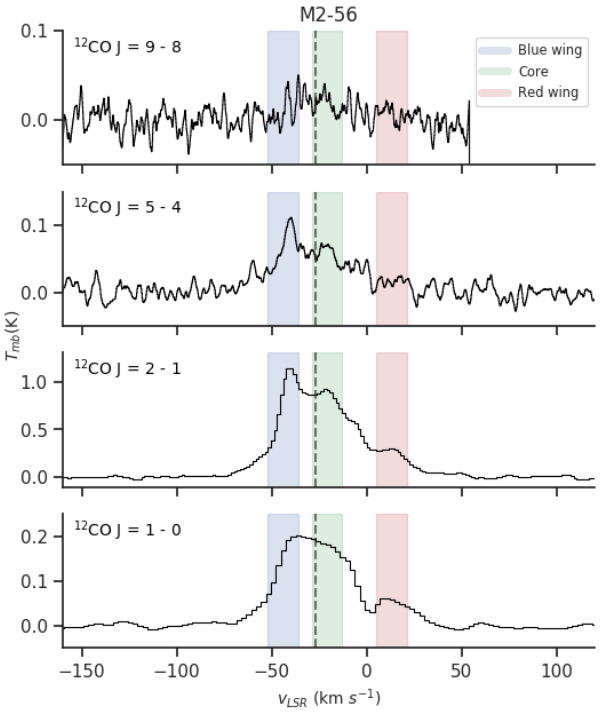


Fig. A.5. Observations of M 2–56. Shadowed regions mark the LSR velocity ranges adopted for each feature and the dashed vertical line indicates the systemic velocity.

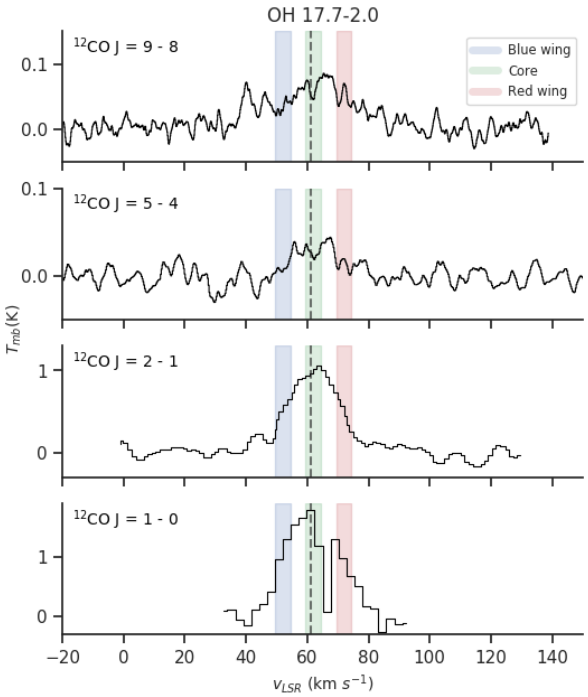


Fig. A.6. Observations of OH 17.7–2.0. Shadowed regions mark the LSR velocity ranges adopted for each feature and the dashed vertical line indicates the systemic velocity.

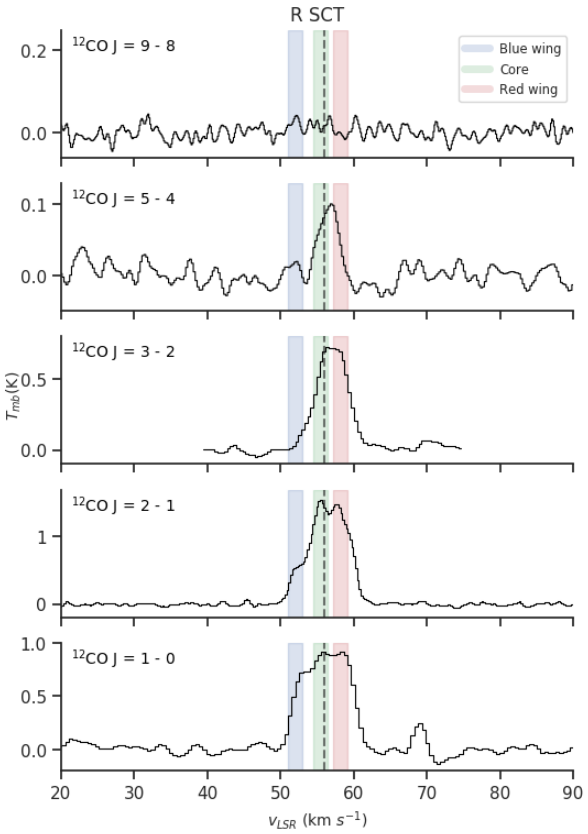


Fig. A.7. Observations of R Sct. Shadowed regions mark the LSR velocity ranges adopted for each feature and the dashed vertical line indicates the systemic velocity. The CO $J = 3$–2 line is taken from De Beck et al. (2010). It is shown here only as an illustration of the line profile evolution between the low- and intermediate-J CO lines, but it will not be used in our quantitative study.

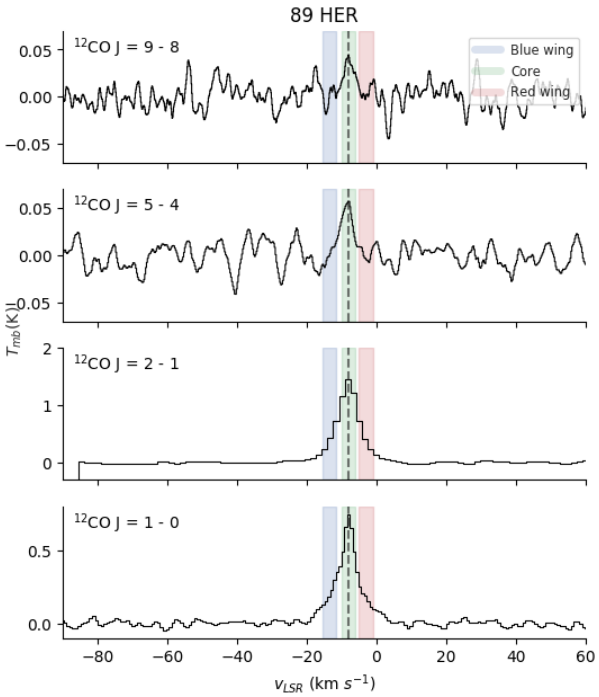


Fig. A.8. Observations of 89 Her. Shadowed regions mark the LSR velocity ranges adopted for each feature and the dashed vertical line indicates the systemic velocity.

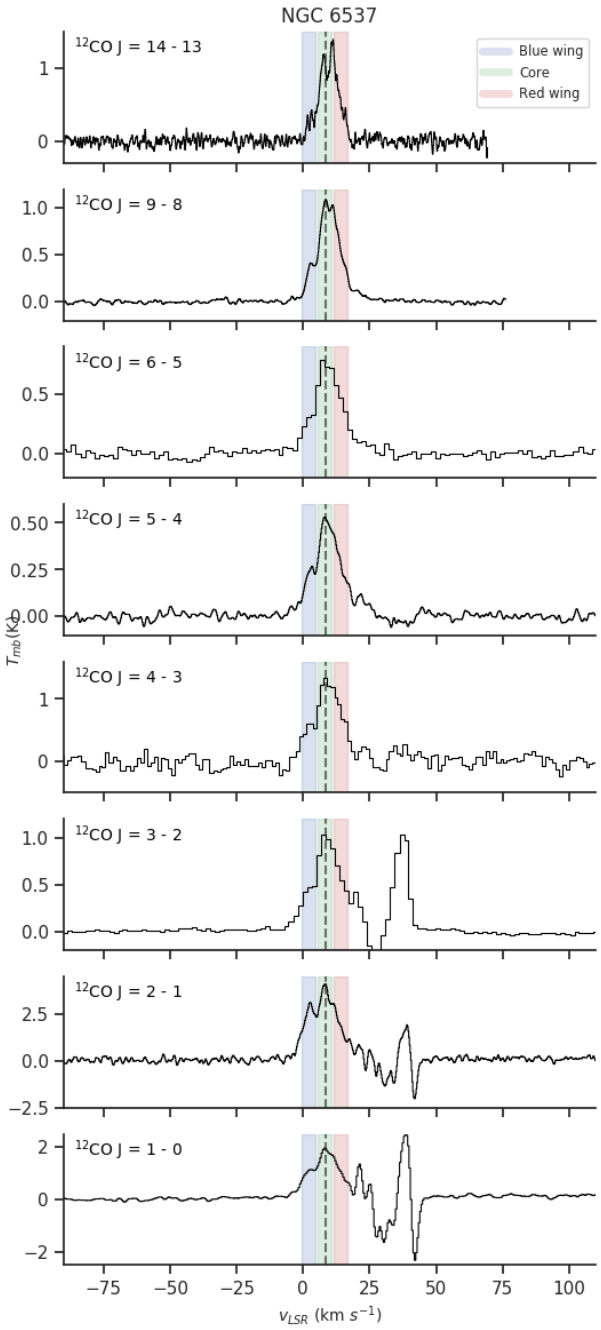


Fig. A.9. Observations of NGC 6537. Shadowed regions mark the LSR velocity ranges adopted for each feature and the dashed vertical line indicates the systemic velocity. The CO $J = 3$–2, $J = 4$–3 and $J = 6$–5 transitions are taken from Edwards et al. (2014). They are shown here just as an illustration of the line profile evolution between the low- and intermediate-J CO lines, but they are used in our quantitative study.

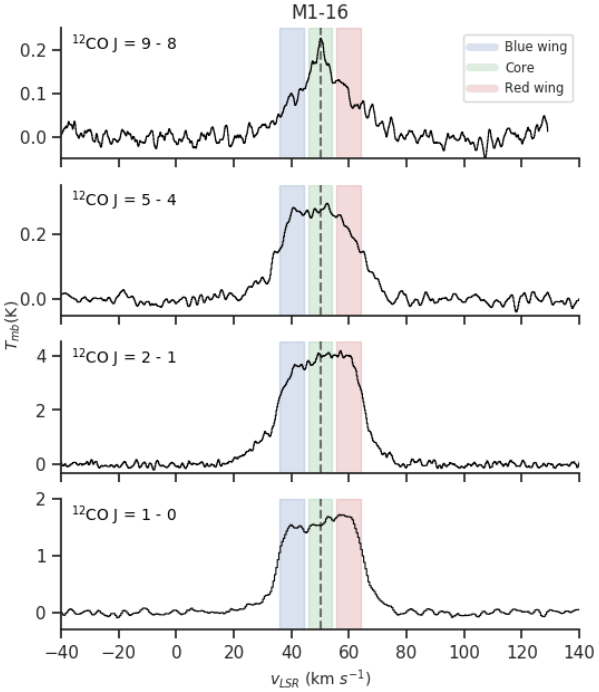


Fig. A.10. Observations of M 1–16. Shadowed regions mark the LSR velocity ranges adopted for each feature and the dashed vertical line indicates the systemic velocity.

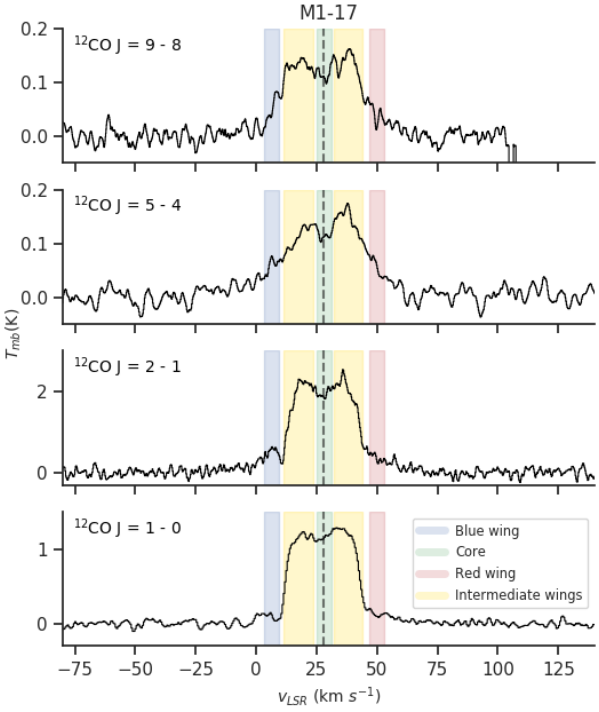


Fig. A.11. Observations of M 1–17. Shadowed regions mark the LSR velocity ranges adopted for each feature and the dashed vertical line indicates the systemic velocity. See Sect. 4.4 for the reference to the intermediate wings.

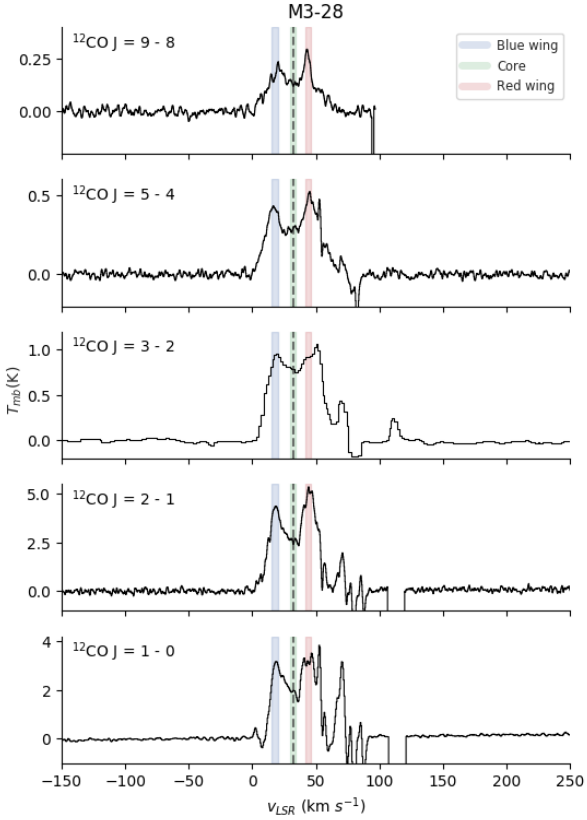


Fig. A.12. Observations of M 3–28. Shadowed regions mark the LSR velocity ranges adopted for each feature and the dashed vertical line indicates the systemic velocity. The CO $J = 3$–2, transitions is taken from Schmidt & Ziurys (2016). It is shown here just as an illustration of the line profile evolution between the low- and intermediate-J CO lines, but is not used in our quantitative study.

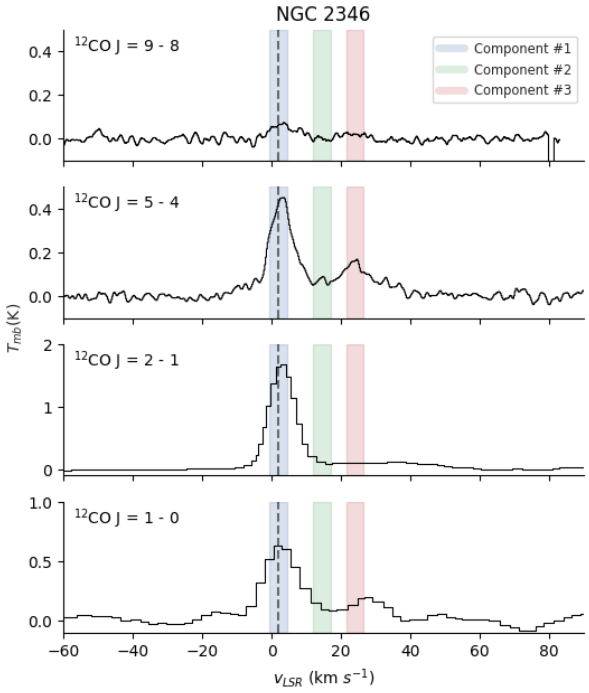


Fig. A.13. Observations of NGC 2346. Shadowed regions indicate the velocity ranges adopted for the detected velocity components and the dashed line marks the systemic velocity.

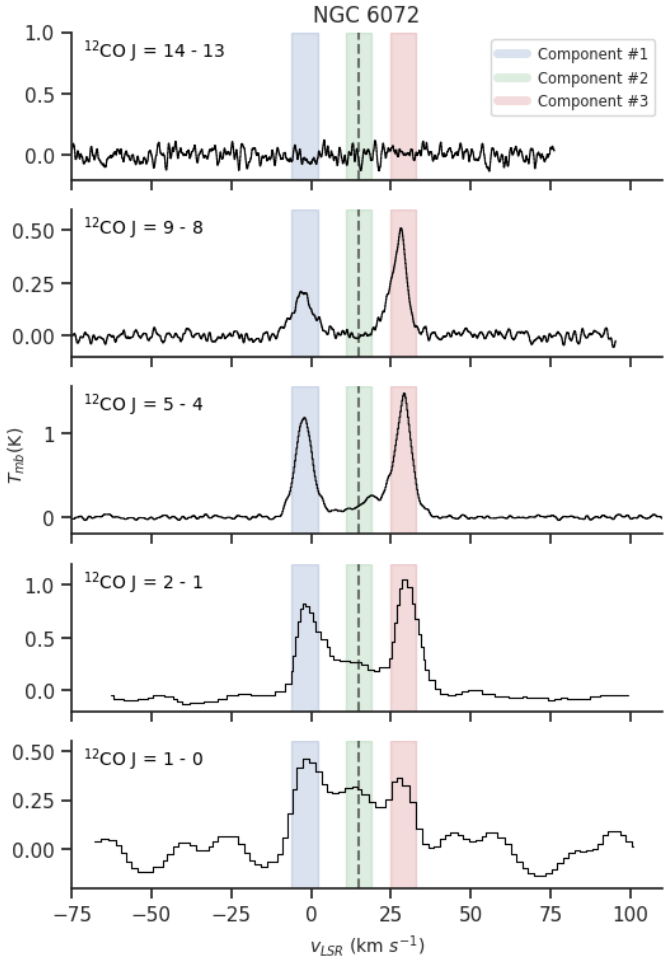


Fig. A.14. Observations of NGC 6072. Shadowed regions indicate the velocity ranges adopted for the detected velocity components and the dashed line marks the systemic velocity.

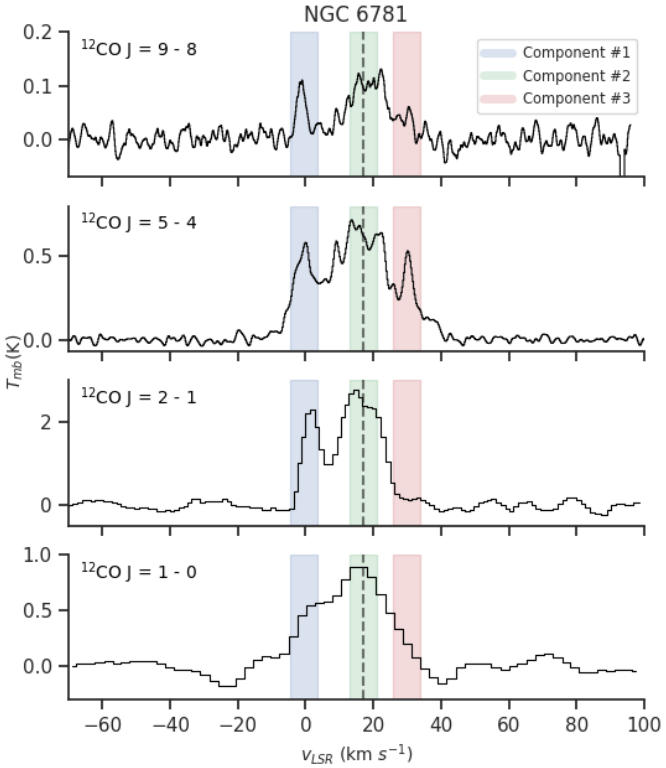


Fig. A.15. Observations of NGC 6781. Shadowed regions indicate the velocity ranges adopted for the detected velocity components and the dashed line marks the systemic velocity.

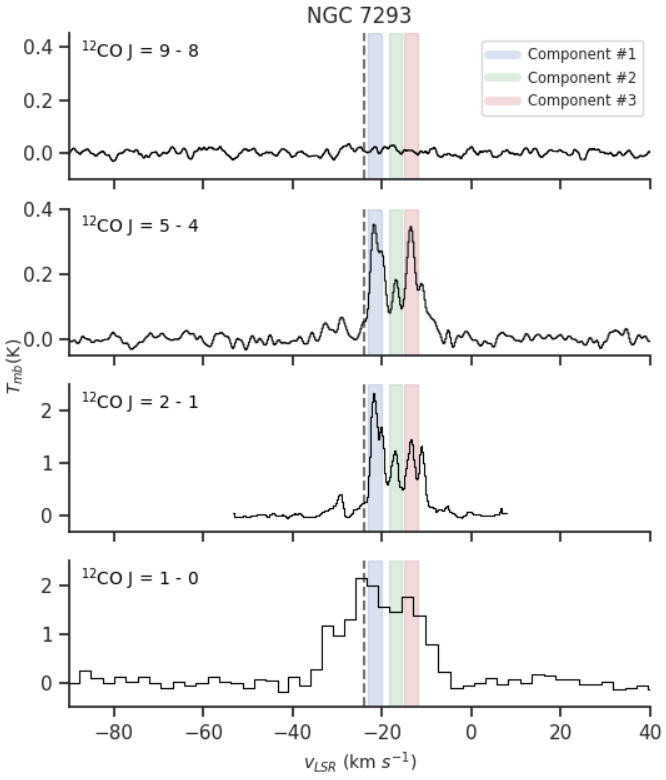


Fig. A.16. Observations of NGC 7293. Shadowed regions indicate the velocity ranges adopted for the detected velocity components and the dashed line marks the systemic velocity.

Appendix B: Optical and FIR images of the sample

In this section, we present the optical and FIR images (when available) of our targets. The *Herschel*/HIFI beams of the lines used in this work are overlayed on these maps red contours, in order of size from largest to smallest: ^{12}CO $J = 5$–4, ^{12}CO $J = 9$–8 and ^{12}CO $J = 14$–13.

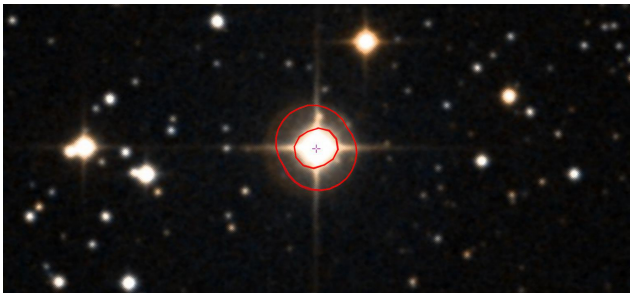


Fig. B.1. Image of IRAS 07134+1005 obtained from DSS2 colour.

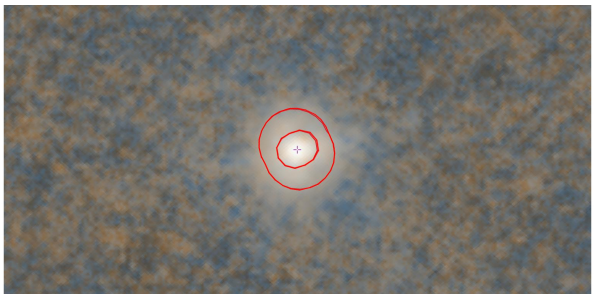


Fig. B.2. FIR image of IRAS 07134+1005 obtained by *Herschel* PACS RGB 70 160 microns.

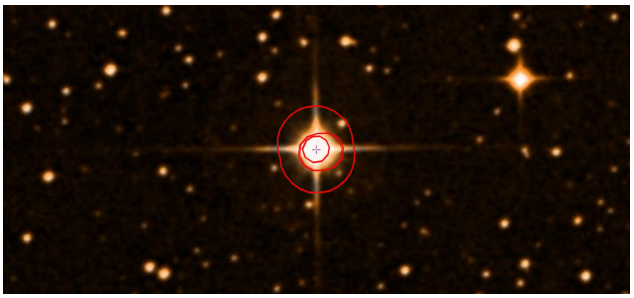


Fig. B.3. Image of IRAS 19500–1709 obtained from DSS2 colour.

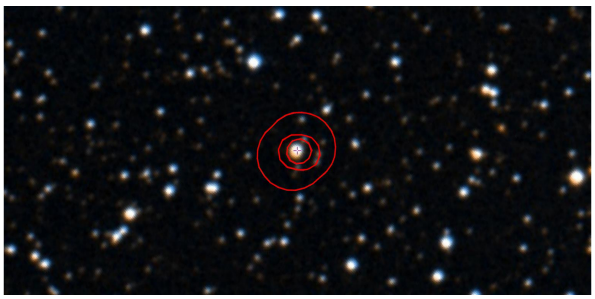


Fig. B.4. Image of IRAS 21282+5050 obtained from DSS2 colour.

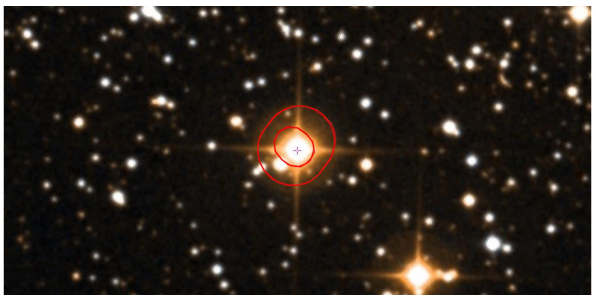


Fig. B.5. Image of IRAS 22272+5435 obtained from DSS2 colour.

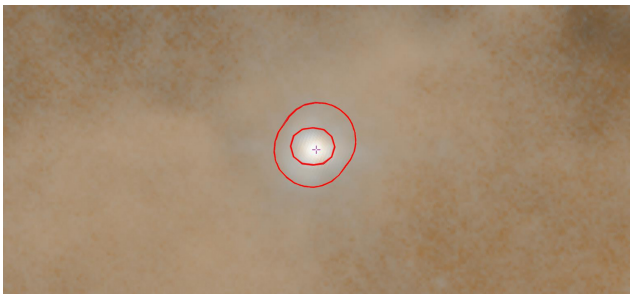


Fig. B.6. FIR image of IRAS 22272+5435 obtained by *Herschel* PACS RGB 70 160 microns.

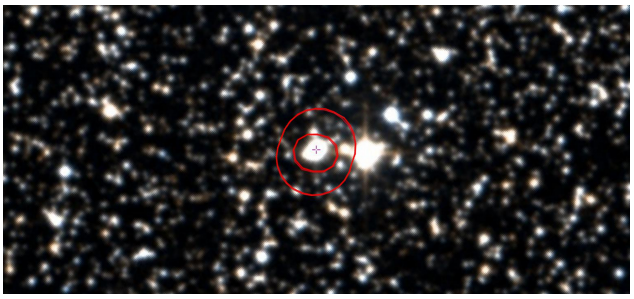


Fig. B.7. Image of M 1–92 obtained from DSS2 colour.

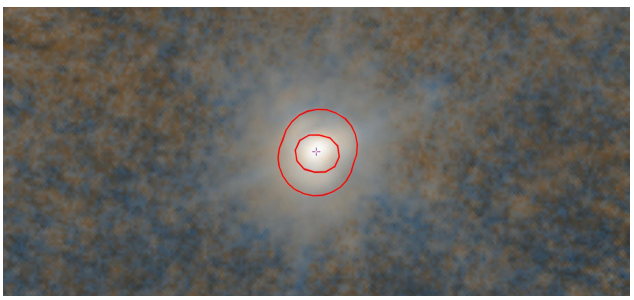


Fig. B.8. FIR image of M 1–92 obtained by *Herschel* PACS RGB 70 160 microns.

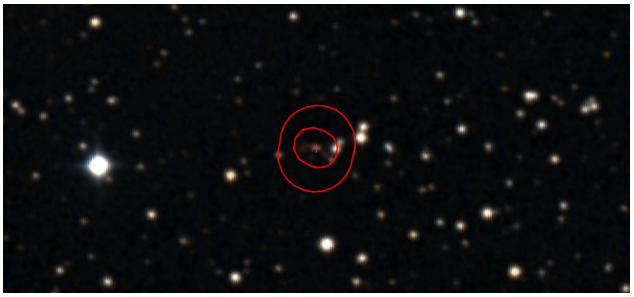


Fig. B.9. Image of M 2–56 obtained from DSS2 colour.

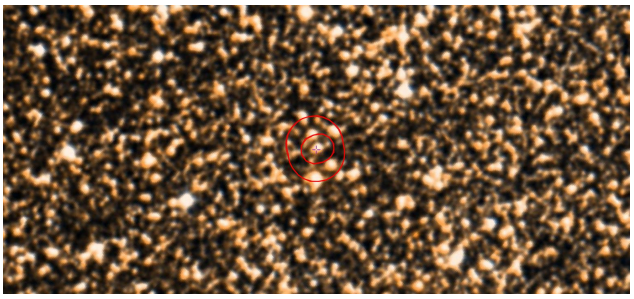


Fig. B.10. Image of OH 17.7–2.0 obtained from DSS2 colour.

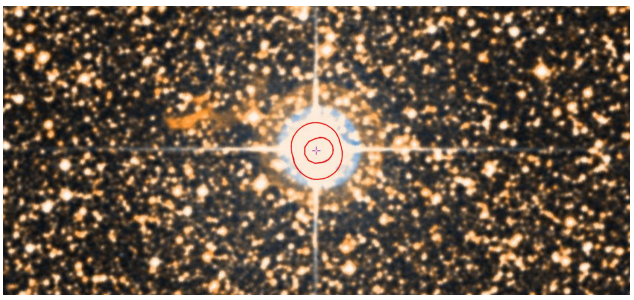


Fig. B.11. Image of R Sct obtained from DSS2 colour.

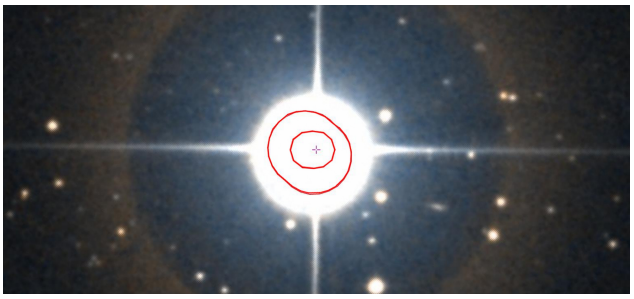


Fig. B.12. Image of 89 Her obtained from DSS2 colour.

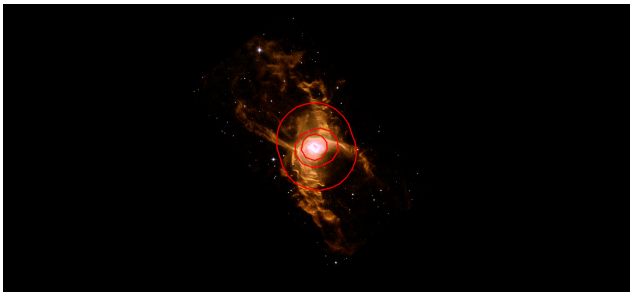


Fig. B.13. NASA/ESA *Hubble* Space Telescope image of NGC 6537, a composite of [N II] 6584 Å (red), Hα 6563 Å (green), and [O III] 5007 Å (blue) emission.

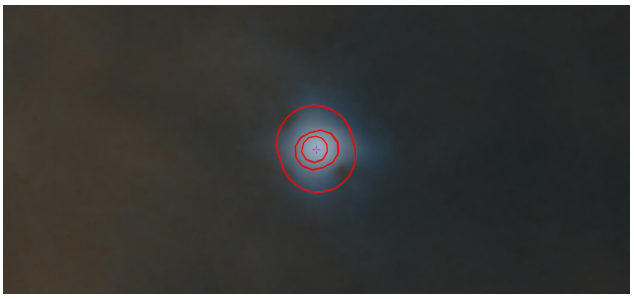


Fig. B.14. FIR image of NGC 6537 obtained by *Herschel* PACS RGB 70,160 microns.

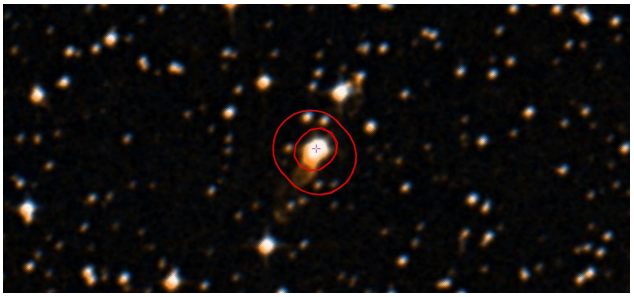


Fig. B.15. Image of M 1–16 obtained from DSS2 colour.

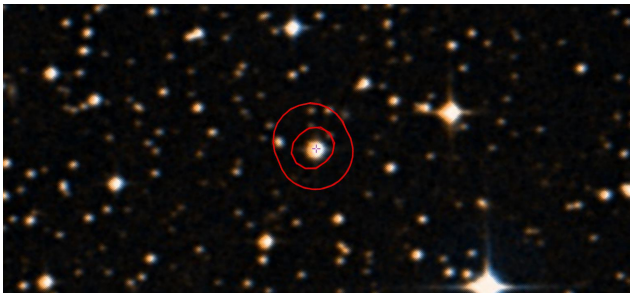


Fig. B.16. Image of M 1–17 obtained from DSS2 colour.

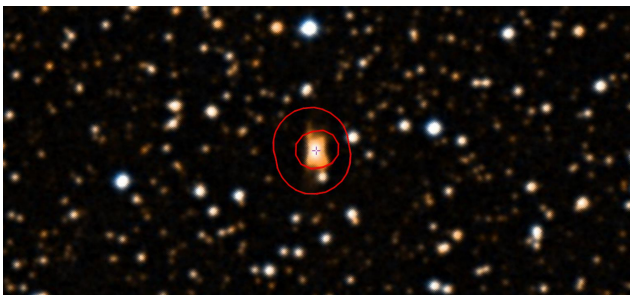


Fig. B.17. Image of M 3–28 obtained from DSS2 colour.



Fig. B.18. FIR image of M 3–28 obtained by *Herschel* PACS RGB 70,160 microns.



Fig. B.19. Composite image of NGC 6072, Hα (red), [OIII] (green), B filters (blue), produced by Ganymed Telescope.

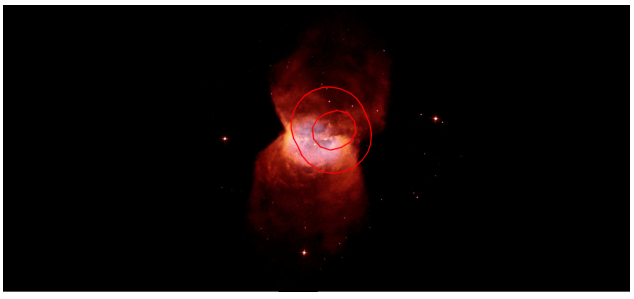


Fig. B.20. NASA/ESA *Hubble* Space Telescope image of NGC 2346, a composite of R band 6750 Å (red), Hα 6560 Å (green), [SII] 6730 Å (blue).

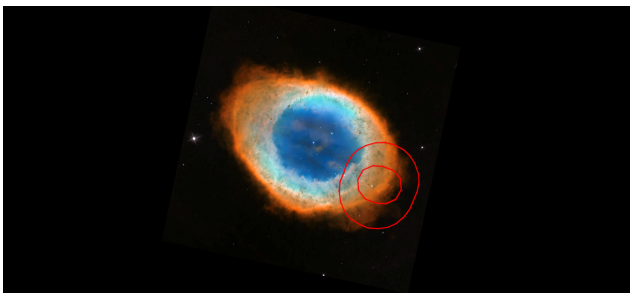


Fig. B.21. NASA/ESA *Hubble* Space Telescope image of NGC 6720, a composite of R filters 6580 Å and 6730 Å (red), G filters 6560 Å and 6450 Å and V filters 5020 Å (green), B filters 4690 Å and 4870 Å (blue).

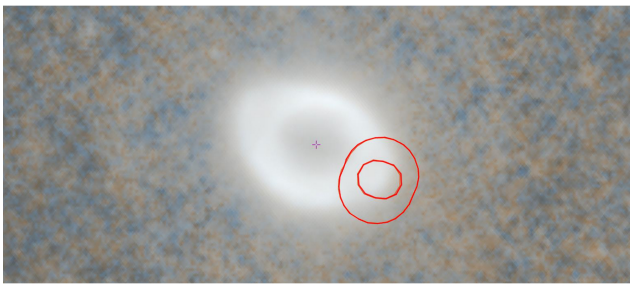


Fig. B.22. FIR image of NGC 6720 obtained by *Herschel* PACS RGB 70 160 microns.

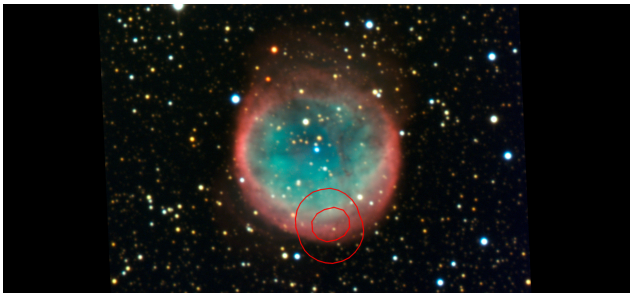


Fig. B.23. ESO image of NGC 6781, a composite of R and Hα (red), V band and [OIII] (green), *B* band (blue).

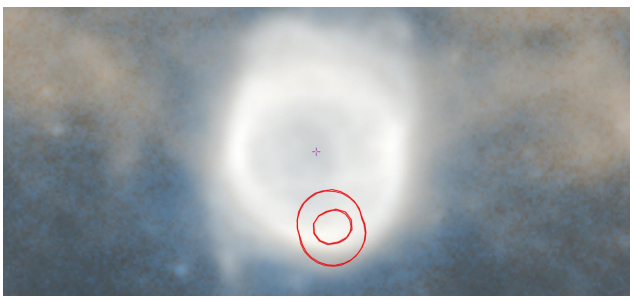


Fig. B.24. FIR image of NGC 6781 obtained by *Herschel* PACS RGB 70 160 microns.



Fig. B.25. Image of NGC 7293 obtained from DSS2 colour.

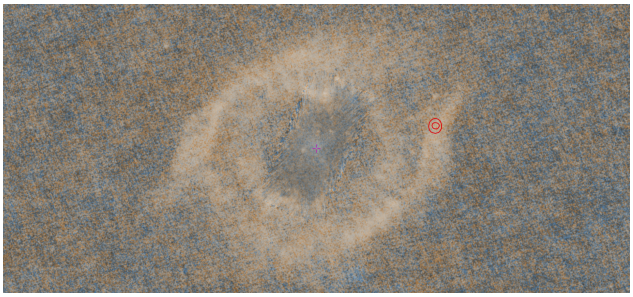


Fig. B.26. FIR image of NGC 7293 obtained by *Herschel* PACS RGB 70 160 microns.